POLITECNICO DI TORINO

Master's Degree in Aerospace Engineering

Master's Degree Thesis

3D Beamforming Algorithm for Vehicle Aeroacoustic Investigation

Supervisors:

Prof. Francesco Avallone

Ing. Alessandro Aquili

Ing. Francesco Uffreduzzi

Candidate:

Elena Tumino

April 2025

Abstract

The significant reduction in automotive powertrain noise, due to electric vehicles and stringent emissions regulations, has highlighted wind noise and its mitigation as a key area of automotive development. Consequently, the precise identification of aeroacoustic noise sources is vital for enhancing vehicle acoustic comfort in a cost-effective and efficient manner, particularly as many of the noise sources now observed were once masked by powertrain sounds.

Currently, beamforming techniques, which utilize one or more microphone arrays to detect noise sources on a virtual plane near the vehicle, are the industry standard for external aeroacoustic assessment. However, assuming that all noise sources reside on this defined plane can lead to inaccuracies in estimating the intensity and location of off-plane sources. To address this limitation, Pininfarina has implemented a multi-plane approach for its overhead microphone array. This strategy defines several planes that more accurately capture the vehicle's vertical dimensions, with the natural evolution of this method being the direct mapping of noise sources onto a three-dimensional scan of the vehicle.

This thesis aims to develop a new algorithm that merges data from three arrays into a single acoustic map of the vehicle's surface using a Multiplicative Beamforming technique. This approach minimizes localization errors and inaccuracies in source strength caused by focus deviations.

Table of Contents

List of Tables

List of Figures

Chapter 1

Introduction

1.1 Overview

The transition to electric vehicles and more stringent emission standards have radically changed the focus of automotive acoustics research over the last two decades. Wind noise has become an issue due to the significant reduction in powertrain noise in electric vehicles, and it is therefore important to understand and control aeroacoustic noise sources to ensure that vehicles are comfortable and efficient. It is therefore essential to identify and control the aeroacoustic noise sources so that the acoustic performance of the vehicle becomes competitive without compromising the efficiency of the design process. With the increasing complexity of vehicle shapes, classical noise assessment methods cannot be applied to three-dimensional objects and complex noise sources. However, to meet these challenges, motivated by academic and industrial requirements, new advanced measurement methods have been developed to capture the complexity of the acoustic response of modern vehicles.

In wind tunnel conditions, acoustic source localisation has historically been carried out using techniques such as elliptical mirrors [1]. These devices work on the concept of spatial filtering, using mirrors to direct the acoustic energy from a particular source to a particular focus. The elliptical mirror technique was implemented based on the far-field formulation of acoustic propagation as acoustic rays to perform Fourier analysis on the received signals to quantify the noise power as a function of frequency. The main drawback of this approach was that it had some practical limitations. The method required high mechanical precision and long sampling times; in addition, the high storage costs of the traversing systems and the specialised equipment required made this method unsuitable for large-scale industrial application.

The mid-1990s saw the advent of digital computing, high-speed data acquisition systems and improved data storage, which changed the world of acoustic measurement [1].The development of very sophisticated microphone array techniques, using more than a hundred digital sensors, greatly improved the robustness and spatial resolution of acoustic source mapping. This was made possible by the use of miniaturised digital microphones first developed for the telecommunications and smartphone industries. The use of these microphones led to a sharp reduction in the cost per channel due to economies of scale and improvements in digital multiplexing. As a result of these technological improvements, not only have the spatial resolution and reliability of acoustic maps in wind tunnels and outdoor environments been improved, but beamforming techniques have also been made available to small and medium sized companies involved in product development and noise control.

Beamforming methods are widely used in various applications such as aeroacoustic characterisation of aircraft and trains, noise assessment of helicopters and jet engines. These methods work by designing directional spatial filters using an array of microphones to separate and measure noise sources to produce acoustic maps that have a main lobe that points to the source and side lobes that are the remaining artifacts of beamforming. The spatial resolution of these acoustic maps is limited by the width of the main lobe and the side lobes, which can mask the signal from weaker sources in the presence of stronger sources. The accuracy of source localisation is largely influenced by the point spread function (PSF) of a beamformer, which is a function of the number of microphones, array geometry, aperture size, frequency content and the characteristics of the filters used. DAMAS (Deconvolution Approach for the Mapping of Acoustic Sources) and CLEAN-SC (Clean based on Source Coherence) are examples of advanced deconvolution techniques that have been proposed to address the blurring effects of the PSF and increase the accuracy of the acoustic maps [2]. Under difficult measurement conditions, these techniques have been shown to significantly improve the ability to separate and measure the levels of multiple nearby noise sources.

However, while beamforming techniques have brought about several improvements, the limitations of planar beamforming are most evident in the complex geometries of modern vehicles. The projection of acoustic data onto a single virtual plane leads to many misinterpretations of the location and intensity of noise sources [2], especially for components that are not parallel to the measurement plane, such as overhead structures or curved surfaces. To overcome these problems, Pininfarina introduced multi-plane beamforming formulations.

Pininfarina's approach to approximating the three-dimensional shape of vehicles using multiple parallel virtual planes was designed to increase the spatial correspondence between the mapping surface and the source locations. Although the use of multi-plane mapping was an improvement over purely planar methods, it was still an approximation; the simplification of representing a three-dimensional surface as a few two-dimensional slices cannot capture the complexity of real-world vehicle topologies and out-of-plane effects.

In response to the persistent limitations of both planar and multi-plane methods, three-dimensional beamforming has been developed, directly mapping acoustic sources onto the vehicle's surface using high-resolution 3D scans. This innovative technique eliminates the need for planar approximation by integrating the actual geometric contours of the vehicle into the analysis, thereby enhancing the accuracy of noise source localization and the estimation of their acoustic strength by accounting for the complete surface topology. This enhanced precision is of particular value in the context of modern electric vehicles, where even minor inaccuracies in noise mapping can impede the development of effective noise reduction strategies.The approach involves integrating data from multiple microphone arrays into a unified acoustic map, which is then projected onto a detailed three-dimensional model of the vehicle.This unified mapping provides a more precise representation of the aeroacoustic environment and streamlines the evaluation process in wind tunnel tests, reducing both time and cost. In essence, 3D beamforming establishes a direct correlation between the measured acoustic data and the actual vehicle geometry, thereby facilitating a more intuitive comprehension of the manner in which airflow interacts with complex surfaces to generate noise.

In summary, the rapid evolution of automotive acoustics research from the early elliptical acoustic mirrors to modern 3D beamforming techniques is in line with advances in both hardware and signal processing. As electric vehicles gradually eliminate conventional powertrain noise and change the acoustic environment, the accurate mapping of wind noise on complex vehicle geometries becomes increasingly important. This paper describes the application of a new 3D beamforming technique that combines data from multiple microphone arrays and presents the results of acoustic mapping in a single map superimposed on the vehicle surface. This method, which overcomes the limitations of planar and multi-plane methods, greatly improves the reliability and accuracy of wind tunnel evaluations and could be a useful practical tool for improving vehicle acoustic comfort and reducing time to market in a highly competitive market.

1.2 Objectives of the Thesis

The objective of this research is to investigate the potential of 3D beamforming algorithms in the context of vehicle aeroacoustics. To this end, the study will firstly examine the limitations of 2D beamforming techniques, encompassing both planar and multiplane methods. Subsequent experiments and research endeavours will be undertaken to enhance and refine 3D beamforming techniques. The thesis is structured into six primary chapters.

1. The present one, namely the Introduction, introduces the research problem and outlines the objectives of the thesis.

2. Chapter 2 provides a comprehensive review of the theoretical foundations pertinent to the interpretation of the experimental results, and it also presents the beamforming algorithms utilised in this thesis.

3. Chapter 3 provides a comprehensive description of the Pininfarina wind tunnel facility and a detailed characterisation of the experimental measurement instruments utilised.

4. In chapter 4, a detailed comparison is conducted among three beamforming formulations — single-plane, multiplane, and three-dimensional. The analysis focuses on a parametric vehicle model tested in the Pininfarina wind tunnel, which is equipped with two synchronised white noise sources.

5. Chapter 5, the beamforming analysis is expanded from a Pininfarina wind tunnel vehicle parametric model to a real production vehicle case, with the investigation of the aeroacoustic sources.

6. Chapter 6 provides a synopsis of the findings and a discussion of potential avenues for future research.

Chapter 2

Theoretical Background

This chapter provides a thorough review of the theoretical underpinnings and basic principles that underpin the research presented in this thesis. The discussion is divided into two main sections: The first section, entitled 'Linear Acoustics', provides a thorough review of the theoretical underpinnings and fundamental concepts that underpin linear acoustics. The second section, entitled "Beamforming", delves into the intricacies of beamforming techniques and their applications.

Section 2.1 introduces the principles of linear acoustics. It commences with the derivation of the acoustic wave equation and proceeds to examine the sound generation mechanisms associated with a small sphere. The subsequent exploration of the principle of superposition alongside the far field approximations is then followed by an analysis of various sound sources, namely monopole, dipole, and quadrupole sources. This systematic exposition establishes the mathematical and physical foundations and thus provides a foundation for the more advanced discussions that follow.

The formulation of beamforming techniques is the focus of the section 2.2. It starts with the description of Delay-And-Sum Beamforming as the initial approach and further developments. The Pininfarina Conventional Beamforming technique is then introduced, followed by the Multiplicative Beamforming approach developed for three-dimensional scenarios. Figures and equations are used throughout the chapter to aid understanding of the discussion and to relate the information to the established notation and structure.

2.1 Linear Acoustics

Acoustic waves constitute oscillatory disturbances that propagate through an elastic medium, conveying energy without any net displacement of mass. In gaseous media, these minute variations in pressure, density, and velocity travel as longitudinal waves, creating alternating regions of compression and rarefaction. For isentropic disturbances, the speed at which these waves propagate—commonly known as the speed of sound—is defined by

$$c_0 = \sqrt{\left(\frac{\partial p}{\partial \rho}\right)_s}, \tag{2.1}$$

where c_0 represents the speed of sound, p the pressure, and ρ the density.

In the case of an ideal gas, the speed of sound may be expressed as

$$c_0 = \sqrt{\gamma R T}, \tag{2.2}$$

with γ denoting the adiabatic index, R the specific gas constant, and T the absolute temperature. Under standard conditions (e.g., $T = 15°\mathrm{C}$), the value of c_0 is approximately 340 m/s. Moreover, the frequency f of a sound wave is related to its wavelength λ by

$$f = \frac{c_0}{\lambda}. \tag{2.3}$$

Sound is detected by the human auditory system through pressure variations that impinge upon the tympanic membrane. The range of audible frequencies for humans extends from roughly 20 Hz to 20 kHz, with maximum sensitivity occurring between 1 kHz and 5 kHz. Consequently, investigations in acoustics frequently focus on phenomena related to human noise perception.

Since the propagation of sound entails energy transport [3], two primary quantities are defined: the sound power P_w (expressed in Watts) and the sound intensity I, which is the power per unit area (W/m^2). As indicated in Table 2.1, the span of sound power levels is extremely broad, necessitating the use of a logarithmic scale for their representation.

Type of Sound	$\mathbf{P_W}$ [W]
Whisper	10^{-10}
Scream	10^{-5}
Jet engine	10^{5}
Rocket engine	10^{7}

Table 2.1: Sound power levels for various sound types.

The sound power level (PWL) is defined in decibels (dB) as

$$\mathrm{PWL} = 10 \log_{10}\left(\frac{P_w}{P_{w,\mathrm{ref}}}\right), \tag{2.4}$$

where $P_{w,\mathrm{ref}}$ is a reference sound power.

Similarly, the sound pressure p' is defined as the deviation in pressure relative to a specified reference value. For a periodic signal with period T, its effective, or root mean square (RMS), value is given by

$$\langle p'^2 \rangle = p'^2_{\mathrm{rms}} = \frac{1}{T} \int_{t_0-T/2}^{t_0+T/2} p'^2(t)\, dt. \tag{2.5}$$

Owing to the wide dynamic range of pressure variations, the sound pressure level (SPL) is likewise expressed on a logarithmic scale:

$$\mathrm{SPL} = 10 \log_{10}\left(\frac{p'^2_{\mathrm{rms}}}{p^2_{\mathrm{ref}}}\right) = 20 \log_{10}\left(\frac{p'_{\mathrm{rms}}}{p_{\mathrm{ref}}}\right), \tag{2.6}$$

where p_{ref} is typically taken as $20\,\mu$Pa in air, corresponding to the threshold of human hearing. Inverting this relationship yields

$$p'_{\mathrm{rms}} = p_{\mathrm{ref}}\, 10^{\mathrm{SPL}/20}. \tag{2.7}$$

Furthermore, it is common practice to apply a frequency weighting to p'_{rms} to account for the varying sensitivity of human hearing across different frequencies. The weighted RMS pressure is defined as

$$\left(p'^2_{\mathrm{rms}}\right)_w = W(f)\, p'^2_{\mathrm{rms}}, \tag{2.8}$$

with the weighting function specified by $W(f) = 10^{\Delta L_w(f)/10}$.

2.1.1 The Acoustic Wave Equation

Acoustic wave propagation in a continuous medium is fundamentally described by the complete Navier–Stokes equations. However, for most common and industrial sound levels (typically below 130 dB), the disturbances are so small that the propagation may be assumed to be linear and isentropic [4]. Under these circumstances, the otherwise complex governing equations can be considerably simplified, leading to both the linear acoustic wave equation and its frequency-domain equivalent, the Helmholtz equation.

To obtain these simplified models, one begins by assuming that the medium is initially at rest and exhibits uniform, time-invariant properties. In this setting, the acoustic pressure p' and density ρ' are regarded as small perturbations around the equilibrium state [5], so that the total pressure and density are expressed as

$$p = p_0 + p', \quad \rho = \rho_0 + \rho',$$

with $p' \ll p_0$. In many instances, the perturbations satisfy

$$\frac{\rho'_{\mathrm{rms}}}{\rho_0} = \frac{p'_{\mathrm{rms}}}{\rho_0 c_0^2} = \frac{p'_{\mathrm{rms}}}{\gamma p_0} \lesssim 10^{-3},$$

where $c_0 = \sqrt{\gamma p_0/\rho_0}$ (for example, $\rho_0 = 1.225$ kg/m^3, $\gamma = 1.4$, and $c_0 \approx 338$ m/s). This smallness condition justifies the linearization of the full equations.

By substituting $\rho = \rho_0 + \rho'$ into the continuity equation

$$\frac{\partial \rho}{\partial t} + \nabla \cdot (\rho\,\mathbf{v}) = 0, \tag{2.9}$$

and neglecting nonlinear terms, one obtains the linearized continuity equation

$$\frac{\partial \rho'}{\partial t} + \rho_0\,\nabla \cdot \mathbf{v} = 0. \tag{2.10}$$

Similarly, by omitting viscous effects and the nonlinear convective terms in the momentum equation, the linearized momentum equation becomes

$$\rho_0\,\frac{\partial \mathbf{v}}{\partial t} + \nabla p' = \mathbf{0}. \tag{2.11}$$

Differentiating Eq. (2.10) with respect to time and then subtracting the divergence of Eq. (2.11) yields

$$\frac{\partial^2 \rho'}{\partial t^2} - \nabla^2 p' = 0. \tag{2.12}$$

By applying the isentropic relation $p' = c_0^2\,\rho'$, this equation can be recast as the homogeneous acoustic wave equation

$$\frac{1}{c_0^2}\,\frac{\partial^2 p'}{\partial t^2} - \nabla^2 p' = 0. \tag{2.13}$$

Together, Eqs. (2.11) and (2.13) constitute the basis of linear acoustics in a stationary medium with uniform properties.

In many practical applications, however, it is necessary to account for the generation of sound by a source. For example, when an elementary monopole source is present, the wave equation is augmented by a forcing term:

$$\left(\frac{1}{c_0^2}\frac{\partial^2}{\partial t^2} - \nabla^2\right) p(\mathbf{x}, t) = q(t)\,\delta(\mathbf{x} - \mathbf{x}_0), \tag{2.14}$$

where $q(t)$ quantifies the source strength and $\delta(\mathbf{x}-\mathbf{x}_0)$ is the Dirac delta function that locates the source. Under free-field conditions, the solution to Eq. (2.14) is given by

$$p(\mathbf{x}, t) = \frac{1}{4\pi}\,\frac{q\Big(t - |\mathbf{x} - \mathbf{x}_0|/c_0\Big)}{|\mathbf{x} - \mathbf{x}_0|}. \tag{2.15}$$

This expression emphasizes two fundamental aspects of acoustic propagation: (i) the amplitude decays inversely with the distance from the source, and (ii) the acoustic pressure at time t corresponds to the source output at the retarded time

$$t_0 = \frac{|\mathbf{x} - \mathbf{x}_0|}{c_0}, \tag{2.16}$$

thereby accounting for the finite speed of sound.

Often, interest lies in characterizing a sound field as a function of frequency rather than time. To do so, one may consider a harmonic signal of the form $f(t) = A\cos(\omega t - \Phi)$. In this situation, a solution to Eq. (2.13) is given by

$$p'(r, t) = \frac{A\cos(\omega t - \omega r/c_0 - \Phi)}{r}, \tag{2.17}$$

where A and Φ are real constants that determine the amplitude and phase of the wave, respectively.

It is often advantageous to represent a harmonic time series as the real part of a complex exponential $e^{-i\omega t}$. With this approach, Eq. (2.17) may be rewritten as

$$p'(r, t) = \mathrm{Re}\left[\hat{p}(r)e^{-i\omega t}\right] = \mathrm{Re}\left[\frac{\hat{A}e^{-i\omega t + ikr}}{r}\right], \tag{2.18}$$

where the symbol $\hat{A}$ denotes a complex amplitude defined by $\hat{A} = A\exp(i\Phi)$, and $k = \omega/c_0$ is the acoustic wavenumber. For brevity, the time dependence is often suppressed, leading to the notation

$$\hat{p}(r) = \frac{\hat{A}e^{ikr}}{r}. \tag{2.19}$$

More generally, the linear acoustic wave equation (2.13) can be reformulated in terms of the complex pressure amplitude $\hat{p}(\mathbf{x})$ by assuming

$$p'(\mathbf{x}, t) = \mathrm{Re}\left[\hat{p}(\mathbf{x})e^{-i\omega t}\right],$$

which leads directly to the Helmholtz equation:

$$\nabla^2\hat{p} + k^2\hat{p} = 0. \tag{2.20}$$

2.1.2 Sound generation by a small sphere

In addressing a sound radiation or scattering problem, the initial step is to select an appropriate solution of the wave equation, following which the relevant boundary conditions are applied to evaluate any undetermined constants, such as the constant $\hat{A}$ as demonstrated in Eq. 2.19. To illustrate this procedure,consider the sound emission from a small pulsating sphere of radius a, which exhibits a normal surface velocity of $u_0e^{-i\omega t}$, as depicted in Fig. 2.1.

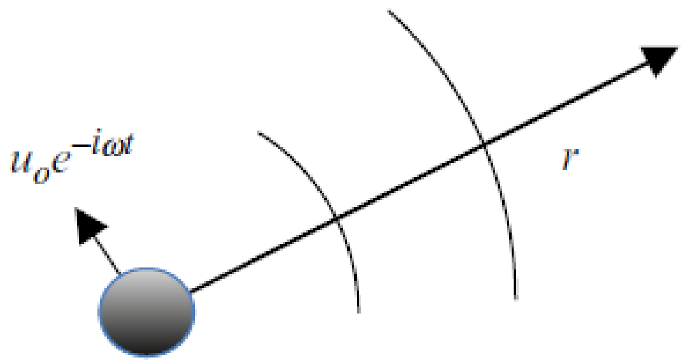

Figure 2.1: A small sphere with a radial surface velocity [5]

In this instance, the valid solution of the wave equation that complies with the boundary condition is presented in Eq. 2.19. The unknown constant $\hat{A}$ is then determined by equating the particle velocity in the radial direction is equated to the surface velocity, namely, $[\hat{\nu_r}]_{r=a} = u_0$, and subsequently applying the acoustic momentum equation, $i\omega\rho_0\hat{\mathbf{v}} = \nabla\hat{p}$:

$$\left[\frac{1}{i\omega\rho_0}\frac{\partial\hat{p}}{\partial r}\right]_{r=a} = u_0 \tag{2.21}$$

From Eq. 2.19, the following expression can be deduced:

$$\frac{\partial \hat{p}(r)}{\partial r} = -\frac{\hat{A}(1 - ikr)e^{ikr}}{r^2} \tag{2.22}$$

At the sphere's surface, that is, when $r = a$, the following condition holds:

$$\left[\frac{\partial \hat{p}(r)}{\partial r}\right]_{r=a} = -\frac{\hat{A}(1 - ika)e^{ika}}{a^2} \tag{2.23}$$

By inserting this result into Eq. 2.21 and solving for $\hat{A}$, the value of the constant is determined.

$$\hat{A} = -\frac{i\omega\rho_0 a^2 u_0 e^{-ika}}{(1 - ika)} \tag{2.24}$$

The complete solution for the acoustic field is then given by Eq. 2.19 as

$$\hat{p} = -\frac{i\omega\rho_0 a^2 u_0 e^{-ik(r-a)}}{(1 - ika)r} \tag{2.25}$$

It is important to note that when the sphere is sufficiently small (i.e., $ka \ll 1$), the exponential term e^{-ika} can be approximated by $1 - ika$, leading to a simplified form of the solution.

$$\hat{p} = -\frac{i\omega\rho_0 a^2 u_0 e^{-ikr}}{r} \tag{2.26}$$

Eq. 2.25 illustrates that the acoustic field in the domain is governed exclusively by boundary conditions. Since a harmonic time dependence was assumed, no initial conditions were necessary. It should also be noted that the surface area of the sphere is given by $S = 4\pi a^2$, and one can express the rate of change in the volume of the sphere as

$$Qe^{-i\omega t} = u_0 S e^{-i\omega t} \tag{2.27}$$

so

$$\hat{p} = -\frac{i\omega\rho_0 Q e^{-ikr}}{4\pi r} \tag{2.28}$$

Consequently, the acoustic pressure is directly linked to the rate at which the volume changes due to the surface displacement. For this reason, a sphere undergoing radial pulsations is commonly identified as a volume displacement source. It is also referred to as a simple source or an acoustic monopole, since the resulting sound field depends only on the distance from the sphere's center. Furthermore, the term $\rho_0 Q e^{-i\omega t}$ physically represents the "rate of change of mass" of the fluid displaced by the surface movement.

In the resolution of the wave equation, the propagation of sound waves through the medium was characterized, and by imposing the boundary conditions, the initiation of these waves was determined. This solution is valid exclusively for the specific boundary motion described here. For example, if the surface were an ellipsoid, the solution to the wave equation would have to be formulated in ellipsoidal coordinates, a considerably more complex task. Other shapes necessitate the solution of the wave equation in different orthogonal coordinate systems, and only a limited number of these systems admit analytical solutions. Thus, this approach addresses only a finite set of problems, with numerical methods required for arbitrary geometries. An illustrative case that allows an exact solution is that of a sphere oscillating along the x_1 direction with a velocity of $\nu_o e^{i\omega t}$, as shown in Fig. 2.2.

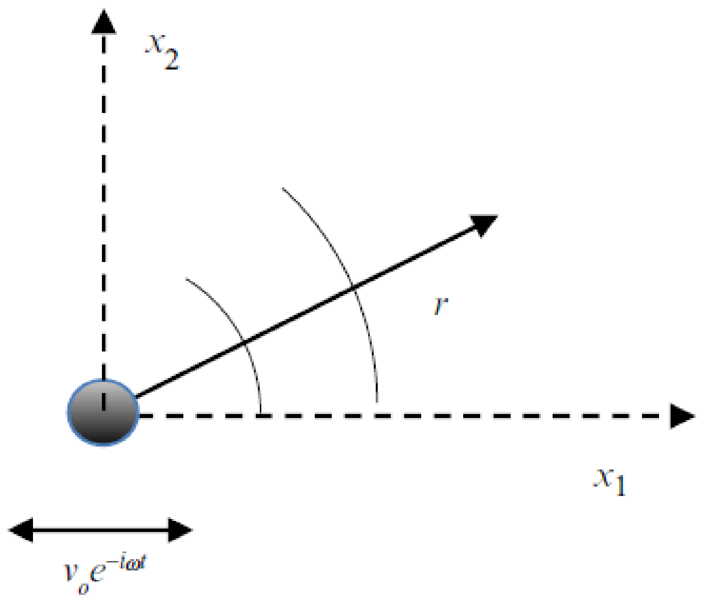

Figure 2.2: Sound radiation from a translating sphere [5]

In this case, the radial component of the surface velocity, perpendicular to the sphere's surface, serves as the essential boundary condition. The tangential component is disregarded due to the omission of viscous effects. Thus, the surface velocity is expressed as

$$[\hat{\nu}_r]_{r=a} = \nu_0 \cos\theta,$$

where θ is the angle between the point on the surface and the x_1 axis. To address this situation, a solution to the wave equation that adheres to this boundary condition is required. This is achieved by differentiating Eq. 2.19 with respect to the x_1 direction, yielding

$$\hat{p}(r) = \frac{\partial}{\partial x_1}\left(\frac{\hat{A}e^{ikr}}{r}\right) \tag{2.29}$$

It can be demonstrated that this differentiated expression is indeed a solution to the wave equation, since any derivative of a solution to the wave equation remains a solution (see the homogeneous acoustic wave equation, Eq. 2.13). Evaluating the derivative in Eq. 2.29 results in

$$\hat{p}(r) = \frac{\partial}{\partial x_1}\frac{\partial}{\partial r}\left(\frac{\hat{A}e^{ikr}}{r}\right) \tag{2.30}$$

Furthermore, considering that

$$r = \sqrt{x_1^2 + x_2^2 + x_3^2},$$

it follows that

$$\frac{\partial r}{\partial x_1} = \frac{x_1}{r} = \cos\theta.$$

Substituting into the derivatives in Eq. 2.30 yields

$$\hat{p}(r) = ikcos\theta\left(\frac{\hat{A}e^{ikr}}{r}\right)\left(1 - \frac{1}{ikr}\right) \tag{2.31}$$

This solution exhibits a $\cos\theta$ directional dependence, which is employed to match the boundary condition for the translating sphere. It is also observed that the amplitude of the sound field is not solely a function of $1/r$; an additional factor of $1/(ikr)$ appears in the solution. This extra term is negligible at distances where $kr \gg 1$ but becomes dominant in regions with $kr \ll 1$. Hence, the domain where $kr \gg 1$ is defined as the acoustic far field, in which the sound wave's amplitude diminishes inversely with distance from the source.

Evaluating the radial component of the acoustic momentum equation,

$$\nabla\hat{p} = i\omega\rho_0\hat{\mathbf{v}},$$

yields

$$\frac{\partial \hat{p}}{\partial r} = i\omega\rho\hat{\mathbf{v}} \cdot \mathbf{n} \tag{2.32}$$

Here, **n** denotes a unit vector pointing radially outward from the sphere's surface. At the boundary, where

$$\hat{\mathbf{v}} \cdot \mathbf{n} = \nu_0 \cos\theta,$$

Gives

$$\left[\frac{1}{i\omega\rho_0}\frac{\partial \hat{p}}{\partial r}\right]_{r=a} = \frac{cos\theta}{\rho_0 c_0}\left(\frac{\hat{A}e^{ika}}{a}\right)\left(ik - \frac{2}{a} + \frac{2}{ika^2}\right) = \nu_0 cos\theta \tag{2.33}$$

For a sphere of sufficiently small dimensions (i.e., when $ka \ll 1$), the approximate solution for the acoustic field can be obtained by retaining only the dominant term $2/(ika^2)$. By solving for $\hat{A}$ and substituting into Eq. 2.31, the following result is obtained:

$$\hat{p}(r) = ikcos\theta\left(\frac{i\omega\rho_0\nu_0 a^3 e^{ikr}}{2r}\right)\left(1 - \frac{1}{ikr}\right) \tag{2.34}$$

The presence of a $\cos\theta$ factor indicates that the acoustic field generated by the translating sphere is primarily directed along the x_1 axis and vanishes in directions perpendicular to the motion. This behavior contrasts with that of a uniformly pulsating sphere, as described in Eq. 2.26, which produces an omnidirectional field. It is also noted that, if u_0 and ν_0 are assumed to be equal, the peak pressure associated with the translating sphere is reduced by a factor of $ka/2$ relative to that of the pulsating sphere at the same distance. Since $ka \ll 1$, the sound levels radiated by the translating sphere for a given surface velocity are considerably lower than those from the pulsating sphere.

The physical rationale behind this observation is that the pulsating sphere displaces a certain mass of fluid during each cycle, compelling the medium to propagate this displacement as an acoustic wave. In contrast, the translating sphere does not induce any net mass displacement; rather, the fluid in the near field adjusts to accommodate the motion. Nevertheless, a fraction of the energy still escapes as sound, propagating into the acoustic far field.

2.1.3 Superposition and Far Field Approximations

The acoustic wave equation (Eq. 2.13) is linear, which implies that the principle of superposition is applicable. Consequently, the overall acoustic field can be represented as the sum of the individual fields generated by distinct sources. To illustrate this concept, consider a configuration of N monopole sources located at positions $\mathbf{y}^{(n)}$, with $n = 1,2,\ldots,N$, as depicted in Fig. 2.3. Accordingly, the total pressure field at an observation point $\mathbf{x}$ is given by

$$\hat{p}(\mathbf{x}) = \sum_{n=1}^{N} \frac{\hat{A}_n\, e^{ik|\mathbf{x}-\mathbf{y}^{(n)}|}}{|\mathbf{x}-\mathbf{y}^{(n)}|}, \tag{2.35}$$

where $\hat{A}_n$ denotes the complex amplitude associated with the n-th source and $|\mathbf{x} - \mathbf{y}^{(n)}|$ represents the distance between the source and the observer.

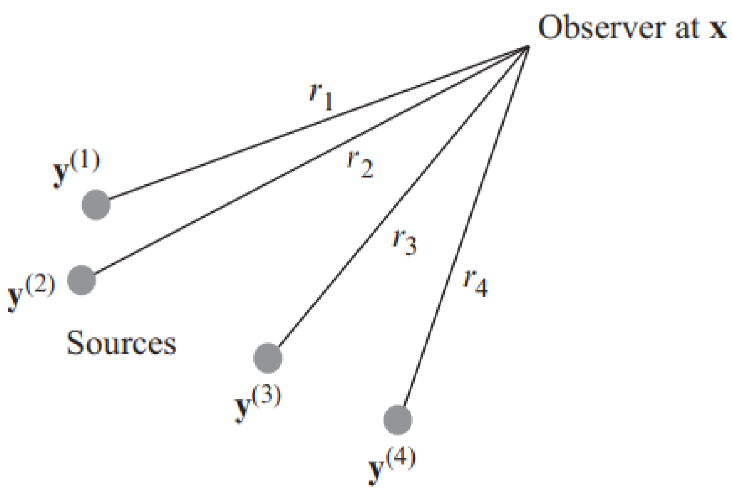

Figure 2.3: Sources distributed over a region [5]

At sufficiently large distances from the sources, this expression can be simplified by expanding $|\mathbf{x} - \mathbf{y}^{(n)}|$ as a Taylor series. In general, one can write

$$|\mathbf{x}-\mathbf{y}| = r(x_i - y_i) = \sqrt{(x_1-y_1)^2 + (x_2-y_2)^2 + (x_3-y_3)^2} \tag{2.36}$$

where $r = r(x_i - y_i)$ explicitly defines the distance from the source to the observer in terms of the coordinates x_i and y_i. By choosing the coordinate origin to lie near the sources, and noting that in the far field $|x| \gg |y|$, the propagation distance may be approximated using a Taylor series expansion.

$$r(x_i - y_i) = r(x_i) - y_i \frac{\partial r(x_i)}{\partial x_i} + \frac{y_i y_j}{2} \frac{\partial^2 r(x_i)}{\partial x_i \partial x_j} + \cdots \tag{2.37}$$

In this expansion, the term $\partial r/\partial x_i = x_i/|\mathbf{x}|$ serves as a direction cosine and is independent of $|\mathbf{x}|$. In contrast, the second-order derivative $\partial^2 r/\partial x_i \partial x_j$

varies inversely with $|\mathbf{x}|$ and thus becomes progressively less significant at large distances from the source.

Retaining the first order terms gives $r(x_i - y_i) = |\mathbf{x}| - x_i y_i/|\mathbf{x}|$, so

$$\hat{p}(\mathbf{x}) \approx \frac{e^{ik|\mathbf{x}|}}{|\mathbf{x}|} \sum_{n=1}^{N} \hat{A}_n \, e^{-ik\,\mathbf{y}^{(n)}\cdot\frac{\mathbf{x}}{|\mathbf{x}|}} \left(1 + \mathbf{y}^{(n)} \cdot \mathbf{x}/|\mathbf{x}|^2\right) \tag{2.38}$$

With $|\mathbf{x}| \gg |\mathbf{y}^{(n)}|$. Consequently, the term

$$\frac{\mathbf{y}^{(n)} \cdot \mathbf{x}}{|\mathbf{x}|^2}$$

within the brackets can be neglected, except in the case—demonstrated later—when the sum of the source amplitudes is zero. However, the dependence on $\mathbf{y}^{(n)}$ within the complex exponential must be retained, as it can dominate the outcome when phase cancellation occurs among the sources. Physically, this effect arises when destructive interference between multiple sources results in a residual sound field that is sensitive to the phase differences among them. The far-field approximation is thus expressed as

$$\hat{p}(\mathbf{x}) \approx \frac{e^{ik|\mathbf{x}|}}{|\mathbf{x}|} \sum_{n=1}^{N} \hat{A}_n \, e^{-ik\,\mathbf{y}^{(n)}\cdot\frac{\mathbf{x}}{|\mathbf{x}|}} \tag{2.39}$$

A crucial aspect of this result is that, in the acoustic far field, the directionality of the field is determined by both the relative positions of the sources and their relative amplitudes, a dependency encapsulated by the unit vector $\mathbf{x}/|\mathbf{x}|$. In this region, the amplitude of the field decays inversely with distance, while the phase increases linearly along surfaces of constant $|\mathbf{x}|$. This finding constitutes an important result that will be extensively utilized in subsequent sections of the text.

This formulation highlights several key features:

- Directional Dependence: The phase term depends on the directional cosines $\mathbf{x}/|\mathbf{x}|$, indicating that the relative positions and strengths of the sources determine the overall directivity of the acoustic field [6].

- Amplitude Decay: The amplitude of the field decays inversely with the distance from the source region, as evidenced by the $1/|\mathbf{x}|$ factor.

- Linear Phase Variation: The phase increases linearly along directions of constant $|\mathbf{x}|$, a property that is fundamental in beamforming and array processing applications [7].

This far-field approximation is widely employed in practical acoustic analyses when the observer is located at a distance much greater than the extent of the source distribution, thus facilitating simplified analytical and numerical evaluations of the sound field.

2.1.4 Monopole, Dipole, and Quadrupole Surces

As noted in Section 2.1.2, a source that produces a simple volume displacement is commonly termed a *monopole*. Its acoustic field is omnidirectional and decays inversely with the distance from the source center. In this section, the discussion turns to multipole sources, which are constructed by combining simple sources of identical magnitude but opposite phase.

The most fundamental example of a multipole source is the *dipole*. This configuration consists of two monopole sources of equal strength and opposing phase, separated by a small distance d (with $kd \ll 1$), as illustrated in Fig. 2.4.

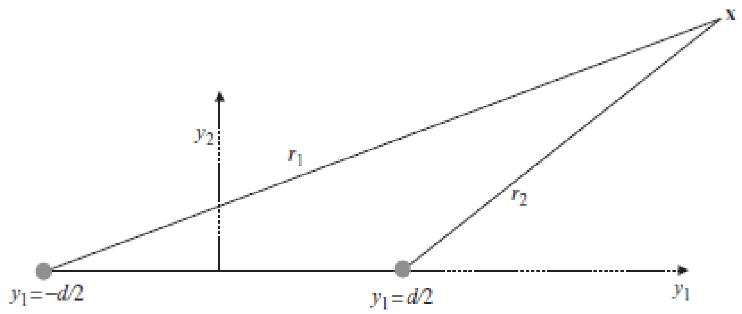

Figure 2.4: Two sources of opposite phase that define a dipole source [5]

The far-field expression for a dipole is derived from Eq. 2.38 by positioning the positive source at $y_1 = -d/2$ and the negative source at $y_1 = d/2$, and by assigning $\hat{A}_1 = i\omega\rho_0 Q/4\pi$ and $\hat{A}_2 = -i\omega\rho_0 Q/4\pi$. Accordingly, one obtains

$$\hat{p}(x) \simeq \frac{i\omega\rho_0 Q e^{ik|\mathbf{x}|}}{4\pi|\mathbf{x}|}\left(e^{ikdx_1/2|\mathbf{x}|}(1 - x_1 d/2|\mathbf{x}|^2 + \cdots) - e^{-ikdx_1/2|\mathbf{x}|}(1 + x_1 d/2|\mathbf{x}|^2 + \cdots)\right) \tag{2.40}$$

under the assumption that $|\mathbf{x}| \gg d$. Given that $kd \ll 1$, the result can be simplified by employing the expansion

$$e^{\pm ikdx_1/2|\mathbf{x}|} = 1 \pm ikdx_1/2|\mathbf{x}| - \frac{1}{2}(kdx_1/2|\mathbf{x}|)^2 + \cdots \tag{2.41}$$

Substituting this expansion into Eq. 2.45 reveals that the zeroth-order terms cancel, leaving

$$\hat{p}(x) \simeq \left(\frac{i\omega\rho_0 Q e^{ik|\mathbf{x}|}}{4\pi|\mathbf{x}|}\right)\left(ikd\frac{x_1}{|\mathbf{x}|} - \frac{x_1 d}{|\mathbf{x}|^2} + \cdots\right), \quad |\mathbf{x}| \gg d \tag{2.42}$$

which may be further simplified by noting that $\cos\theta = x_1/|\mathbf{x}|$. Consequently, one finds

$$\hat{p}(x) \simeq ikdcos\theta\left(\frac{i\omega\rho_0 Q e^{ik|\mathbf{x}|}}{4\pi|\mathbf{x}|}\right)\left(1 - \frac{1}{ik|\mathbf{x}|} + \cdots\right), \quad |\mathbf{x}| \gg d \tag{2.43}$$

The acoustic dipole is characterized by a directional field whose amplitude is modulated by the cosine of the angle between the observer's direction and the line joining the two sources that define the dipole axis. Consequently, its far-field behavior is analogous to that of a transversely oscillating sphere, exhibiting a maximum along the dipole axis and a null at 90° relative to it (see Fig. 2.5). Furthermore, the spatial decay of the field follows a $d/|\mathbf{x}|^2$ dependence when $k|\mathbf{x}| \ll 1$ and a $kd/|\mathbf{x}|$ dependence when $k|\mathbf{x}| \gg 1$, corresponding respectively to the acoustic near-field and far-field approximations. In the far-field regime, the observer must satisfy both the geometric condition $|\mathbf{x}| \gg d$ and the acoustic condition $k|\mathbf{x}| \gg 1$, so that the phase shift due solely to the difference in propagation distances becomes significant.

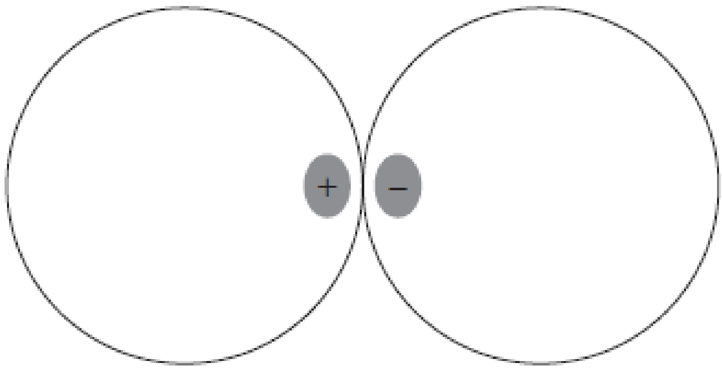

Figure 2.5: The cosine directionality of a dipole source. [5]

It is also important to note that the dipole source has no net volume displacement because the total source strength is zero. Nonetheless, a nonzero acoustic field is produced owing to the finite separation d between the sources. Moreover, the maximum amplitude of the dipole field is ikd times that of the corresponding monopole field at the same distance, and since $kd \ll 1$, the dipole is intrinsically an inefficient radiator of sound.

A *quadrupole* source can be constructed by placing two dipole sources in a back-to-back arrangement, with the positive sources located at $y_1 = -\frac{3d}{2}$ and $y_1 = \frac{3d}{2}$, and the negative sources at $y_1 = -\frac{d}{2}$ and $y_1 = \frac{d}{2}$. Under the acoustic far-field condition ($k|\mathbf{x}| \gg 1$), the net pressure field is given by

$$\hat{p}(x) \simeq \frac{i\omega\rho_0 Q e^{ik|\mathbf{x}|}}{4\pi|\mathbf{x}|}\left(e^{\frac{3ikdx_1}{2|\mathbf{x}|}} - e^{\frac{ikdx_1}{2|\mathbf{x}|}} - e^{-\frac{ikdx_1}{2|\mathbf{x}|}} + e^{-\frac{3ikdx_1}{2|\mathbf{x}|}}\right), \quad |\mathbf{x}| \gg d \tag{2.44}$$

Application of Eq. 2.41 shows that both the zeroth-order and first-order terms in kd cancel, yielding

$$\hat{p}(x) \simeq -2(kd)^2\left(\frac{x_1}{|\mathbf{x}|}\right)^2\frac{i\omega\rho_0 Q e^{ik|\mathbf{x}|}}{4\pi|\mathbf{x}|}, \quad |\mathbf{x}| \gg d,\ k|\mathbf{x}| \gg 1 \tag{2.45}$$

This configuration is known as a longitudinal quadrupole because the sources are collinear and the net volume velocity is zero. The directivity of the quadrupole is governed by a $\cos^2\theta$ factor (as depicted on the left side of Fig. 2.6), and its effective source strength scales with $(kd)^2$, rendering its field an order of magnitude weaker than that of the monopole.

Alternate quadrupole configurations can also be devised. For example, if two sources with amplitude $i\omega\rho_0 Q/4\pi$ are positioned at $y = (d/2, d/2)$ and $y = (-d/2, -d/2)$, while two sources with strength $-i\omega\rho_0 Q/4\pi$ are placed at $y = (d/2, -d/2)$ and $y = (-d/2, d/2)$, then in the acoustic far field the pressure is approximated by

$$\hat{p}(x) \simeq \frac{i\omega\rho_0 Q e^{ik|\mathbf{x}|}}{4\pi|\mathbf{x}|}\left(e^{\frac{ikdx_1}{2|\mathbf{x}|}+\frac{ikdx_2}{2|\mathbf{x}|}} + e^{-\frac{ikdx_1}{2|\mathbf{x}|}+\frac{ikdx_2}{2|\mathbf{x}|}} - e^{\frac{ikdx_1}{2|\mathbf{x}|}-\frac{ikdx_2}{2|\mathbf{x}|}} - e^{-\frac{ikdx_1}{2|\mathbf{x}|}+\frac{ikdx_2}{2|\mathbf{x}|}}\right) \tag{2.46}$$

Then, by employing the expansion

$$e^{-\frac{ikdx_1}{2|\mathbf{x}|}\pm\frac{ikdx_2}{2|\mathbf{x}|}} = 1 - \frac{ikdx_1}{2|\mathbf{x}|} \pm \frac{ikdx_2}{2|\mathbf{x}|} - \frac{1}{2}\left(\frac{kdx_1}{2|\mathbf{x}|} \mp \frac{kdx_2}{2|\mathbf{x}|}\right)^2 + \cdots,$$

The following equation is obtained:

$$\hat{p}(x) \simeq -(kd)^2\frac{i\omega\rho_0 Q e^{ik|\mathbf{x}|}}{4\pi|\mathbf{x}|}\left(\frac{x_1 x_2}{|\mathbf{x}|^2}\right), \quad |\mathbf{x}| \gg d,\ k|\mathbf{x}| \gg 1 \tag{2.47}$$

This result implies a directivity pattern proportional to $\sin\theta\cos\theta$, which is equivalent to $\frac{1}{2}\sin(2\theta)$ (as shown on the right side of Fig. 2.6), with the field magnitude scaling as $(kd)^2$.

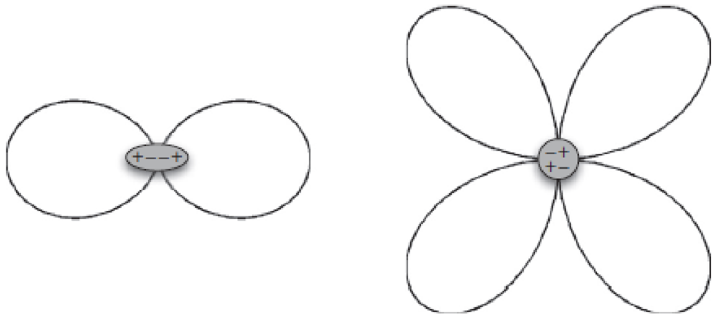

Figure 2.6: The directionality of different types of quadrupole. [5]

2.2 Beamforming

Beamforming is a signal processing technique applied to sensor arrays for localizing and characterizing acoustic sources through phased array principles. Its main objective is to determine the spatial location, intensity, and frequency content of multiple sources simultaneously [8]. Owing to its robustness and accuracy, beamforming is widely used in both research and industrial applications [1].

2.2.1 Delay-And-Sum Beamforming

Delay-and-Sum (DSB) beamforming is one of the simplest and most effective methods for localizing and characterizing acoustic sources. This method, schematically presented in Fig. 2.7, employs an array of m microphones and a defined search grid within the plane presumed to contain the noise source(s). The noise localization process comprises the following steps:

1. A plane is defined to encompass the possible locations of the noise sources, which is then discretized into a grid.

2. Each grid node is examined sequentially. For every node, the signals received by the microphones are delayed according to their respective retarded times $t_0 = |x - x_0|/c$, compensating for propagation differences.

3. The delayed signals from all microphones are summed and normalized by the number of microphones (M) to produce the beamformer output map.

When a noise source aligns with a grid node, constructive interference enhances the beamformer output. Conversely, if no source is present at a given location, phase mismatches lead to signal cancellation, resulting in a low beamformer response, effectively indicating the absence of a source [1].

Once the conceptual framework for Delay-and-Sum Beamforming has been established, the corresponding mathematical analysis is introduced, with the

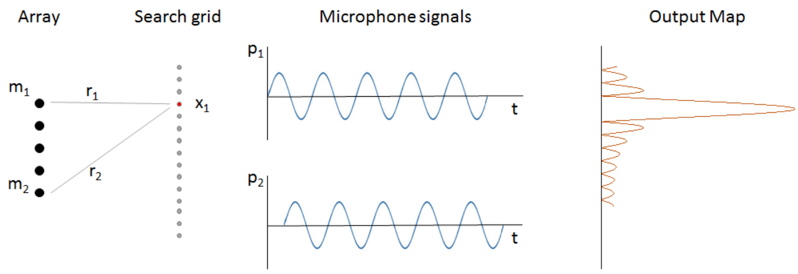

Figure 2.7: Delay-and-Sum Beamforming [1]

formulation derived from the Brüel & Kjær Technical Review [8]. Consider a planar array of M microphones, located at positions $\mathbf{r}_m$ in the xy-plane, as depicted in Fig. 2.8. The pressure signals p_m received by each microphone are individually delayed and then summed:

$$b(\kappa, t) = \sum_{m=1}^{M} w_m p_m(t - \Delta_m(\kappa)) \tag{2.48}$$

Here, w_m denotes the weighting coefficients applied to the microphone signals. In this case, uniform shading is assumed ($w_m \equiv 1$), and therefore these coefficients are omitted in the subsequent discussion. The term Δ_m represents the time delay applied to each microphone, which is adjusted to achieve directional sensitivity towards a specific direction κ. These delays are set so that the signals arriving at the array are aligned in time before being summed. From a geometrical perspective, the time delay is given by:

$$\Delta_m = \frac{\kappa \cdot \mathbf{r}_m}{c} \tag{2.49}$$

where c is the speed of sound. As previously mentioned, signals arriving from other directions will not align coherently and thus will not contribute constructively to the summation, leading to the desired directional sensitivity, as illustrated in Fig. 2.8(b).

In the frequency domain, the output of the beamformer is given by:

$$B(\kappa, \omega) = \sum_{m=1}^{M} P_m(\omega) e^{-j\omega\Delta_m(\kappa)} \tag{2.50}$$

where $P_m(\omega)$ is the Fourier transform of $p_m(t)$, and ω is the angular frequency. Expressing this in terms of the wave vector $\mathbf{k} = -k\kappa$, the beamformer output becomes:

$$B(\kappa, \omega) = \sum_{m=1}^{M} P_m(\omega) e^{-j\mathbf{k}\cdot\mathbf{r}_m}. \tag{2.51}$$

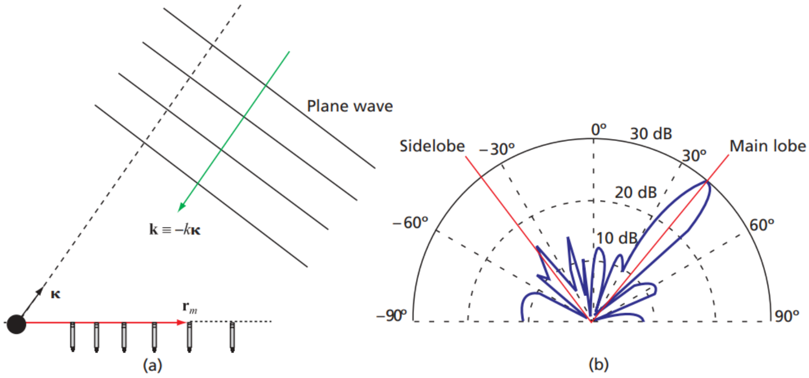

Figure 2.8: (a) A microphone array, a far-field focus direction, and a plane wave incident from the focus direction. (b) A typical directional sensitivity diagram with a main lobe in the focus direction and lower sidelobes in other directions [8]

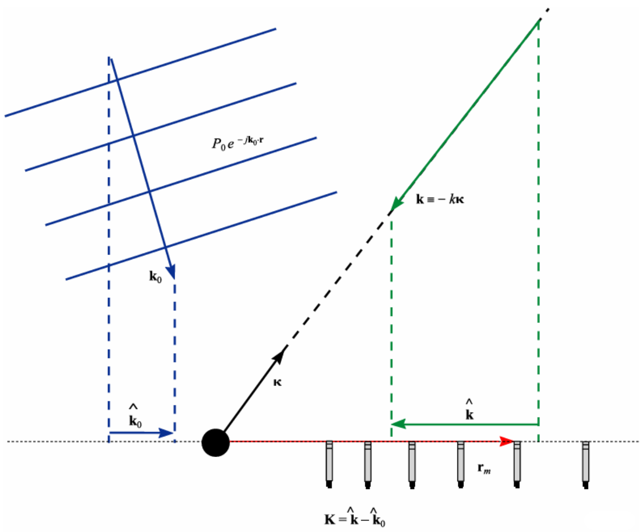

Figure 2.9: A plane wave, with wave number vector $\mathbf{k}_0$, incident from a direction different from the focus direction κ [8].

The selection of time delays $\Delta_m(\kappa)$, or equivalently the "preferred" wave number vector $\mathbf{k} \equiv -k\kappa$, aligns the beamformer toward a specific far-field direction. The goal is to capture only the signals arriving from this direction, ensuring optimal localization of sound sources.

To assess potential leakage from plane waves arriving from other directions, consider a plane wave with a wave number vector $\mathbf{k}_0$ that deviates from the preferred $\mathbf{k}$. The pressure recorded by the microphones is:

$$P_m(\omega) = P_0 e^{-j\mathbf{k}_0 \cdot \mathbf{r}_m} \tag{2.52}$$

which, according to equation (2.51), results in the following beamformer output:

$$B(\kappa,\omega) = P_0 \sum_{m=1}^{M} e^{j(\mathbf{k}-\mathbf{k}_0)\cdot\mathbf{r}_m} \equiv P_0 W(\mathbf{k}-\mathbf{k}_0) \tag{2.53}$$

Here, the function W is the *Array Pattern*, which depends only on the array geometry when $w_m \equiv 1$:

$$W(\mathbf{K}) \equiv \sum_{m=1}^{M} e^{j\mathbf{K}\cdot\mathbf{r}_m}. \tag{2.54}$$

2.2.2 Pininfarina Conventional Beamforming

The Pininfarina Conventional Beamforming algorithm is based on the cross-spectral imaging function with the omission of diagonal terms. In fact, the beamformer filter is realized by calculating the weighted sum of the microphone sound pressures using complex-valued weight factors [8]. Mathematically, this process is described by

$$p_F(x_t) = \mathbf{h}(x_t)^H \mathbf{p}, \tag{2.55}$$

where the vector $\mathbf{h}(x_t)$, known as the steering vector, is determined based on the assumed source position, and the superscript H denotes the Hermitian transpose.

The steering vector is fundamental in defining the beamformer's performance, and it is designed to meet two principal criteria:

- The beamformer should yield a maximal response when the assumed source position coincides with the actual source position.
- The magnitude of the beamformer output should provide a reliable measure of the source strength.

Numerous formulations of the steering vector exist in the literature [2]. One common formulation compensates for both the phase delay and the amplitude attenuation between the presumed noise source and each individual microphone. This formulation is expressed as

$$\mathbf{h}(x_g) = |\mathbf{x}_{\text{Mik}} - \mathbf{x}_g|\, e^{-i\omega t_g}, \tag{2.56}$$

where t_g represents the propagation time from the grid point x_g to the corresponding microphone, and ω is the angular frequency.

Moreover, rather than directly utilizing p_F, one may construct a source map by employing the real-valued autopower spectrum B of the beamformer output:

$$B(\mathbf{x}_t) = E\{p_F(\mathbf{x}_t)p_F^*(\mathbf{x}_t)\} = \mathbf{h}^H(\mathbf{x}_t)E\{\mathbf{p}\mathbf{p}^H\}\mathbf{h}(\mathbf{x}_t) = \mathbf{h}^H(\mathbf{x}_t)\mathbf{G}\mathbf{h}(\mathbf{x}_t), \tag{2.57}$$

with $E\{\cdot\}$ denoting the expectation operator, $(\cdot)^*$ indicating the complex conjugate, and $\mathbf{G}$ representing the cross-spectral matrix of the measured signals.

2.2.3 Multiplicative Beamforming

Multiplicative beamforming is an alternative processing technique developed specifically for three-dimensional (3D) beamforming applications employing non-planar microphone arrays [9]. Unlike conventional planar beamforming methods, which typically process signals from a single array configuration, the multiplicative approach divides the array into multiple subarrays, each covering different spatial orientations. This technique has been shown to improve 3D spatial localization by reducing sidelobe levels and eliminating the directional bias of the main lobe in the beamformer output.

Numerical simulations indicate that multiplicative beamforming enhances the accuracy of source localization, particularly in scenarios involving dipole sound sources commonly encountered in aeroacoustics.

In practice, the multiplicative beamforming technique is implemented by performing conventional beamforming on two or more distinct subarrays, each scanning a 3D grid. For instance, consider an implementation using two mutually perpendicular subarrays, each containing an equal number of microphones. Let the outputs of the two subarrays be defined by

$$B_1(\mathbf{x}_g) = h_1^H(\mathbf{x}_g)\, C_1\, h_1(\mathbf{x}_g)$$

and

$$B_2(\mathbf{x}_g) = h_2^H(\mathbf{x}_g)\, C_2\, h_2(\mathbf{x}_g),$$

where C_1 and C_2 are the cross-spectral matrices corresponding to the first and second subarrays, respectively, and $h_1(\mathbf{x}_g)$ and $h_2(\mathbf{x}_g)$ represent the steering vectors evaluated at the grid point $\mathbf{x}_g$. The final beamformer output is then obtained by taking the square root of the product of these individual outputs:

$$B_t(\mathbf{x}_g) = \sqrt{B_1(\mathbf{x}_g)\, B_2(\mathbf{x}_g)}.$$

The square root operation is critical, as it ensures that B_t accurately represents the true source power when the beamformer is steered to the correct source location.

A significant advantage of multiplicative beamforming is its ability to achieve accurate source localization on complex geometries, such as the surface of a vehicle, while maintaining a limited computational cost. Unlike conventional planar beamforming—where microphone coordinates are referenced to the center of each array independently—the 3D formulation of multiplicative beamforming considers the entire sensor configuration within a global coordinate system. For example, in wind tunnel experiments, the reference system is often defined with its origin at the midpoint of the nozzle exit, thereby ensuring consistency in spatial measurements across the entire array.

In summary, multiplicative beamforming provides a robust and efficient alternative for 3D acoustic source localization, particularly in applications involving non-planar microphone arrays. Its ability to reduce sidelobe interference and correct directional bias makes it especially valuable in challenging aeroacoustic environments.

Chapter 3

Pininfarina Wind Tunnel Facility

With over 50 years of expertise in aerodynamic and aeroacoustic testing, the Pininfarina Wind Tunnel stands as a state-of-the-art facility dedicated primarily to full-scale passenger vehicles. Beyond optimizing aerodynamic performance, a key focus is on aeroacoustic analysis, crucial for enhancing user comfort across various applications, from automotive interiors to architectural structures and marine environments. Leveraging advanced methodologies, including external microphone arrays, beamforming analysis, and calibrated acoustic heads, the facility enables precise identification and characterization of noise sources, both inside and outside the vehicle. This comprehensive approach ensures an in-depth understanding of aeroacoustic phenomena, supporting the development of quieter and more refined designs.

The wind tunnel employs frontal, lateral, and overhead external microphone arrays [10], which have the following characteristics:

- An overhead array, Fig. 3.1 (a), located on the ceiling of the test section (4 m from the floor), which consists of 78 Brüel & Kjær Type 4951 microphones whose specifications are reported in the Tab. 3.1.

- A lateral array,Fig. 3.1 (a), placed on the side wall of the test section, with 66 Brüel & Kjær Type 4951 microphones whose characteristics are the same already introduced in Tab. 3.1.

- A smaller frontal array, Fig. 3.1 (b), installed above the nozzle exit, with 15 Brüel & Kjær Type 4189 microphones whose specifications are summarized in Tab. 3.2.

Sensitivity	6.3 mV/Pa
Frequency	100 Hz – 20 kHz
Dynamic Range	35 – 140 dB
Temperature	-10 °C to +55 °C
Polarization	prepolarized

Table 3.1: Brüel & Kjær 4951 specifications

Sensitivity	50 mV/Pa
Frequency	6.3 Hz – 20 kHz
Dynamic Range	14.6 – 146 dB
Temperature	-30 °C to +150 °C
Polarization	prepolarized

Table 3.2: Brüel & Kjær 4189 specifications

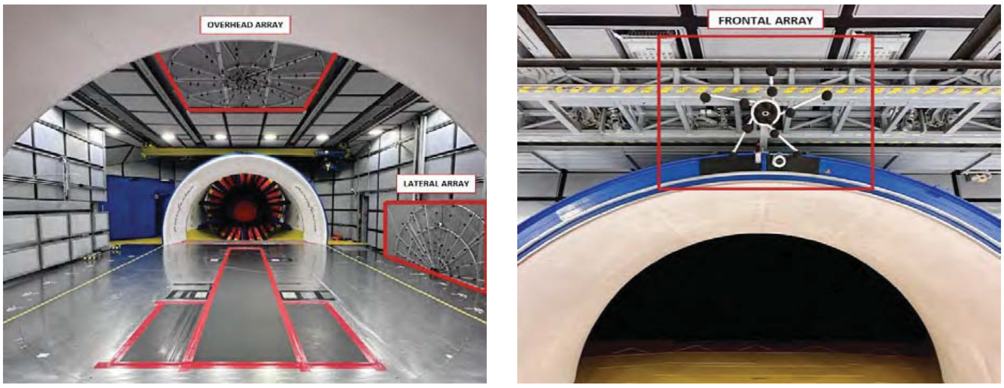

(a) *Pininfarina side and overhead arrays*　**(b)** *Pininfarina frontal array*

Figure 3.1: Pininfarina arrays

3.1 Array Resolution

The resolution of a beamformer indicates its capacity to differentiate between waves arriving from closely spaced directions. For sources in the far field, resolution is defined as the smallest angular separation between two plane waves that allows them to be distinguished. For sources at finite distances, resolution is practically defined as the minimum separation between two sources at which they can still be resolved. Consider two plane waves with wave number vectors $\mathbf{k}_1$ and $\mathbf{k}_2$, $|\mathbf{k}_1| = |\mathbf{k}_2| = k$, incident on a beamformer array characterized by an array pattern W. Assuming both plane waves have unit amplitude, the output of the beamformer is a superposition of the form:

$$B(\kappa, \omega) = W(\mathbf{k} - \mathbf{k}_1) + W(\mathbf{k} - \mathbf{k}_2) \tag{3.1}$$

According to the Rayleigh criterion [11], two directions can be resolved precisely when the peak of $W(\mathbf{k} - \mathbf{k}_2)$ coincides with the first zero of $= W(\mathbf{k} - \mathbf{k}_1)$, as illustrated in Fig. 3.2.

If the angular separation between $\mathbf{k}_1$ and $\mathbf{k}_2$ is minimal, the minimum resolvable source separation in the radial direction $R(\theta)$, at a finite distance z, is given by :

$$R(\theta) = \frac{zR_K}{k} \frac{1}{cos^3\theta} \tag{3.2}$$

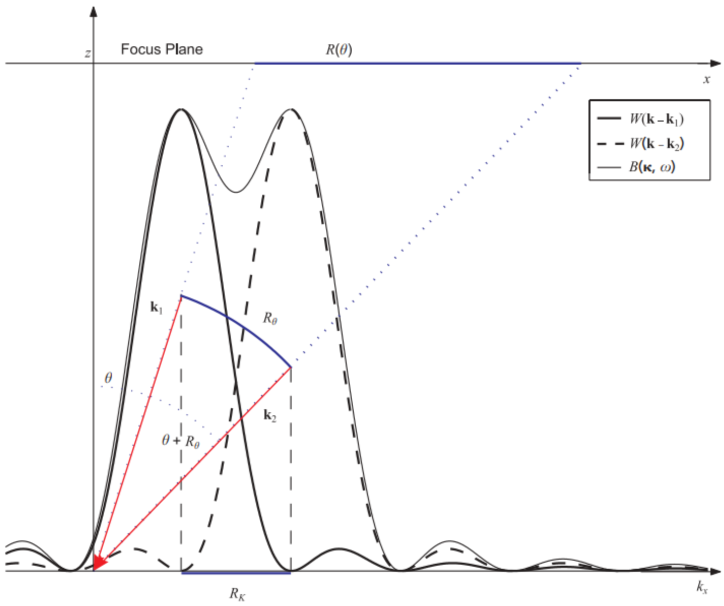

Figure 3.2: The curves show the beamformer output,$B(\kappa, \omega)$, cf. eq.3.1 resulting from two plane waves with wave number vectors $\mathbf{k}_1$ and $\mathbf{k}_2$ incident on a planar array [8]

Where R_K is the main lobe width in the array pattern, that according to the Rayleigh criterion is given by the dirt minimum of the array pattern $R_K = R^0_{min}$; and θ is the off-axis angle.

It is essential to consider that the exact value of R^0_{min} depends on the positions of all array microphones, as described in Eq. 2.54 of the array pattern. A general estimate, however, can be derived by examining limiting cases, such as when an infinite number of transducers is uniformly distributed along a line segment of length D or over a circular disc with radius $D/2$. This scenario assumes continuous sampling of the sound field across the entire aperture, rather than at discrete points. For this continuous case, an integral expression is used for the array pattern in Eq. 2.54, known as the *aperture smoothing function*:

$$W(\mathbf{K}) = \frac{1}{(2\pi)^d} \int_{|\mathbf{r}|<D/2} w(\mathbf{r}) e^{j\mathbf{K}\cdot\mathbf{r}} d^d\mathbf{r} \tag{3.3}$$

Where $d = 1$ for line segment and $d = 2$ for circular aperture and $w(\mathbf{r})$ is a continuous shading function. In case of uniform shading the above equation can be evaluated through the Bessel function of order 1 [11], that allow to find the first zero in the array pattern as:

$$K^0_{min} = \alpha \frac{2\pi}{D} \tag{3.4}$$

Where $\alpha = 1$ for the linear aperture and $\alpha = 1.22$ for the circular aperture. Now, given that the wave number k is related to the wavelength λ by $k = 2\pi/\lambda$, substitution into Eq. 3.2 yields the expression for beamformer resolution:

$$R(\theta) = \frac{\alpha}{cos^3\theta}\frac{z}{D}\lambda \tag{3.5}$$

or on-axis incidence, $\theta = 0$, the resolution is given by:

$$R_{AXIS} = \alpha\left(\frac{z}{D}\right)\lambda \tag{3.6}$$

It is observed that resolution is directly proportional to wavelength and improves with increased aperture size, while it decreases as the distance between array and object increases.

Comparing the on-axis resolution and general off-axis resolution, as per Eqs. 3.6 and 3.5, the ratio between them is given by:

$$\frac{R(\theta)}{R_{AXIS}} = \frac{1}{cos^3\theta} \tag{3.7}$$

This ratio, shown in Fig. 3.3, indicates that for angles of incidence exceeding 30° off-axis, the resolution becomes more than 50% greater than the on-axis resolution, effectively limiting the practical opening angle of the beamformer to 30°

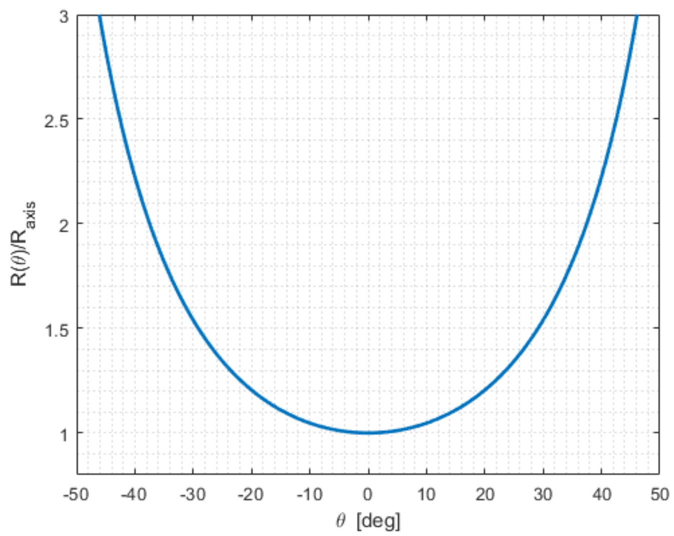

Figure 3.3: variation of the ratio between off-axis and on-axis resolution as given by eq. 3.7

3.2 Array Pattern

The performance of a beamformer array is predominantly determined by its geometry, which defines the beamforming response via the array pattern, gives by the equation 2.54:

$$W(\mathbf{K}) = \sum_{m=1}^{M} e^{j\mathbf{K}\cdot\mathbf{r}_m}, \tag{3.8}$$

where $\mathbf{K} = \mathbf{k} - \mathbf{k}_0$ represents the wave number vector, with $\mathbf{k}$ corresponding to the incident wave from an arbitrary direction and $\mathbf{k}_0$ corresponding to the wave incident from the focal direction. The vector $\mathbf{r}_m$ denotes the position of the m-th microphone.

The spatial arrangement of sensors within the array directly influences spatial sampling, thereby affecting the beamforming system's performance and capabilities. An optimally designed array geometry ensures compliance with the Nyquist criterion and minimizes adverse effects such as spatial aliasing. Hence, precise optimization of the array elements' placement is crucial for achieving high directivity and overall robustness in beamforming applications.

In the case of the Pininfarina array, distinct array patterns are observed across different configurations. The top and side arrays (Fig. 3.5 and 3.4) display similar patterns, each characterized by a markedly pronounced main lobe relative to the sidelobes. Conversely, the front array pattern (Fig. 3.6) exhibits a main lobe that is comparable in magnitude to the sidelobes, a phenomenon attributable to the substantially lower number of microphones in that configuration.

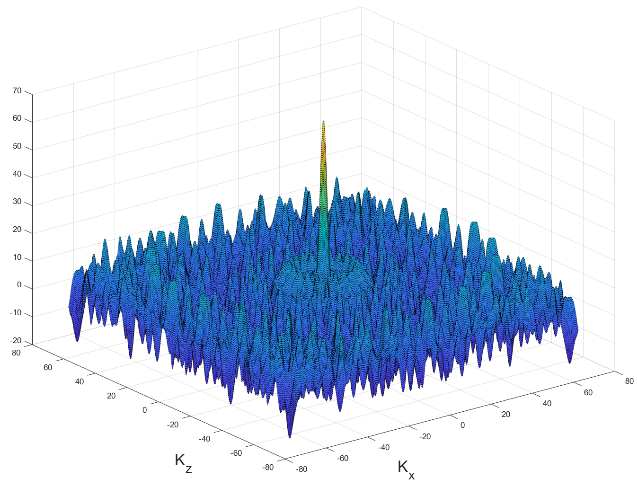

Figure 3.4: Pininfarina Side Array Pattern

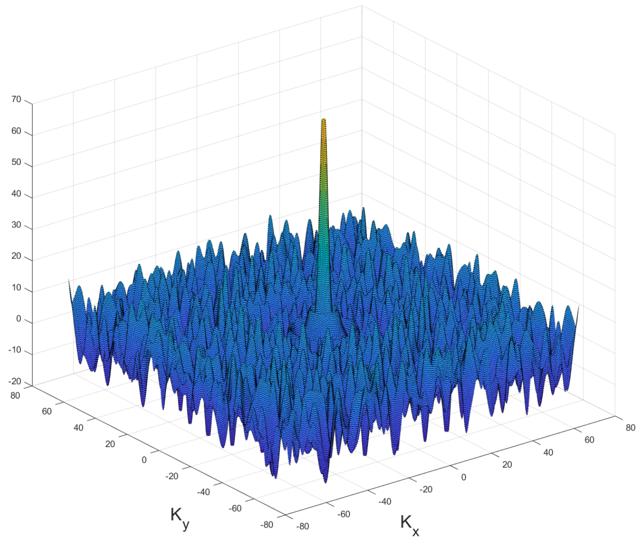

Figure 3.5: Pininfarina Top Array Pattern

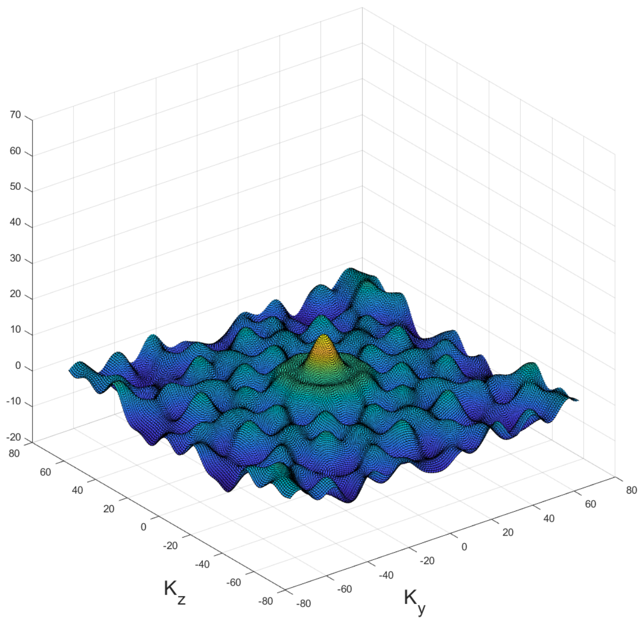

Figure 3.6: Pininfarina Front Array Pattern

3.3 Maximum Sidelobe Levels

The presence of sidelobes in the array pattern (Fig. 3.4 to 3.6) allows waves from off-axis directions to interfere with measurements of the main lobe direction, resulting in false peaks or sources in a measured directional source map. A well-designed phased array is characterized by a low *Maximum Sidelobe Level* (MSL), defined from the radial profile of the array pattern $W_p(K)$, as

$$MSL(K) \equiv maxW_p(K) \equiv 10 \cdot log_{10} \left[max \frac{|W(\mathbf{K})|^2}{M^2} \right] \tag{3.9}$$

Where $|W(\mathbf{K})|$ is the real part of the array pattern equation. Fig. 3.7 shows the result. In accordance with expectations, the top and side arrays exhibit secondary lobes that are considerably smaller than those observed in the front array.

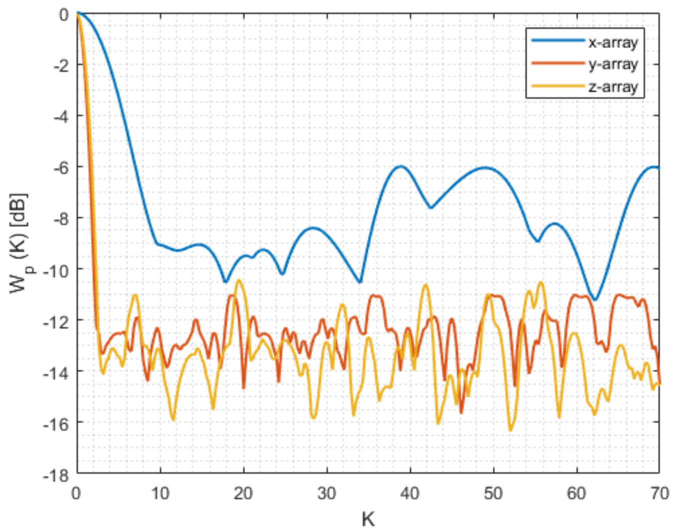

Figure 3.7: Maximum Sidelobe Levels of Pininfarina Arrays

Chapter 4

2D and 3D Beamforming Formulations comparison

The purpose of this chapter is to compare three different beamforming formulations —single-plane, multi-plane, and three-dimensional— and to examine the limitations inherent in two-dimensional approaches.

Conventional beamforming techniques employ microphone arrays to map noise sources onto virtual planes near the vehicle; however, such planar beamforming is inherently constrained when dealing with the complexities of real vehicle geometries, particularly with respect to out-of-plane noise sources, often resulting in the misinterpretation of both the location and intensity of these sources.

To overcome these limitations, Pininfarina initially introduced a multi-plane formulation that approximates the complex vehicle geometry by aligning several virtual planes with potential noise sources. Although this method improves localization, it still falls short of fully capturing the three-dimensional nature of the vehicle's structure.

As a more advanced solution, the three-dimensional beamforming technique maps acoustic sources directly onto the vehicle surface using a 3D scan. Among the various methods proposed in the literature, the Multiplicative Beamforming approach [9] has been implemented here; this method integrates data from multiple microphone arrays into a unified acoustic map projected onto the vehicle surface, thereby eliminating the need for planar approximations or multi-plane techniques. By accurately accounting for the complex surface topology of the vehicle, this approach improves the accuracy of the location of the noise source and the estimation of the strength - a critical improvement in the development of noise reduction strategies for modern electric vehicles, where even small errors can significantly affect overall effectiveness.

4.1 Limitations of 2D Beamforming Formulation

Mapping acoustic data onto a predetermined single plane, often adopted for its apparent computational simplicity, often leads to misinterpretation of both the location and intensity of noise sources, as the chosen plane does not necessarily capture the full three-dimensional propagation of acoustic waves and the complex shape of the vehicle. In ordet to quantitatively assess these limitations, a comprehensive numerical study was carried out using the overhead array configuration.

In this investigation, a monopole noise source, acting as a basic acoustic radiator, was introduced and mathematically characterized by the following equation:

$$p(t) = \frac{\sqrt{2I\rho_0 c}}{r_{\text{mic-source}}} \sin\left[\omega \cdot (t - t_0)\right], \tag{4.1}$$

where $I = 1\ W/m^2$ represents the acoustic intensity, ρ_0 the density of the ambient medium, c the speed of sound, $r_{\text{mic-source}}$ corresponds to the distance between the microphone and the source, and ω represents the angular frequency ($2\pi f$), with f systematically varied over 1, 5, and 10 kHz to investigate the frequency dependence of the observed phenomena. The source was positioned at a distance of 2 meters from the overhead array, as shown in Figure 4.1, which illustrates the geometrical arrangement of the microphones and the source location.

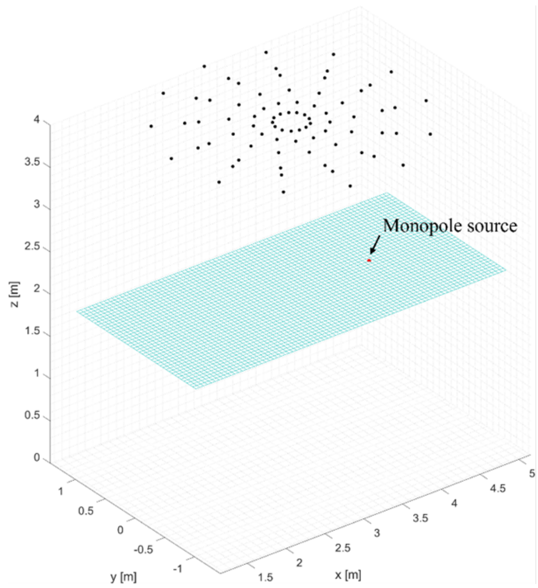

Figure 4.1: Monopole noise source at $z = 2$ m from the overhead array

In order to quantitatively assess the effect of the mismatch between the focal plane and the actual source location, a series of controlled experiments were performed. The z-coordinate of the mapping plane was deliberately modified to emulate scenarios where the assumed source plane is not co-planar with the actual source, while the source was maintained at its reference position. The conventional beamforming algorithm was then applied to determine both the power of the noise source and its spatial coordinates. The results obtained were then carefully compared with the nominal values at different mapping plane distances and source frequencies to determine the effect of the focus plane error on the accuracy of the reconstructed acoustic field, as shown in Figures 1 and 2.

The result of this research is conclusive; even small deviations from the optimum imaging plane can lead to significant errors in source localisation and intensity estimation. For instance, a focal plane error of 500 mm resulted in intensity inaccuracies of up to 12 dB and positioning errors of up to 200 mm. These errors were found to be frequency dependent, with higher frequencies generally resulting in larger errors. The consequences of such deviations can be categorised into two primary effects. Firstly, they affect the accuracy of the generated acoustic map, which can lead to incorrect interpretations of the noise source distributions. Secondly, these errors have the potential to misguide noise control measures, leading to erroneous or misdirected efforts. The primary objective of this paper is to achieve this through the analysis of the experimental data and the interpretation of the results. The results of this research are used to support the hypothesis and justify the initial assumptions. Furthermore, by comparing the results with the literature review, the contribution of this research to the existing knowledge in the field can be assessed.

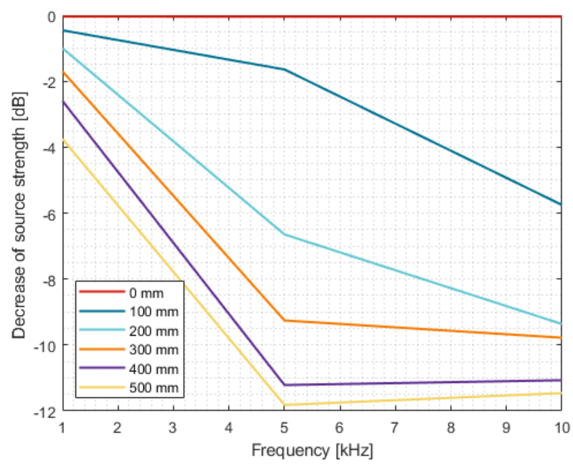

Figure 4.2: Decrease in source strength as a function of focal plane deviation for different source frequencies

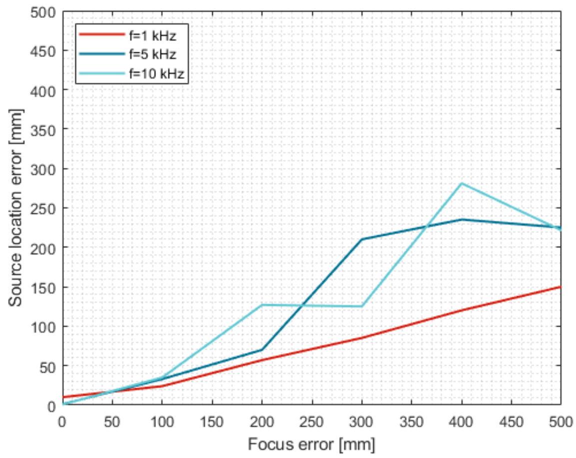

Figure 4.3: Decrease in source location error as a function of focal plane deviation for different source frequencies

The findings outlined in this study elucidate the inherent limitations of two-dimensional beamforming formulations, particularly in scenarios where sources are not confined to the imaging plane. These findings underscore the necessity for three-dimensional approaches that can more accurately represent the actual spatial nature of acoustic sources in real-world vehicular environments. Such environments are often characterised by complexity in geometry, presence of reflection, and the existence of multiple noise sources.

4.2 Validation Case

The purpose of the present section is to provide a comparison of the three different beamforming formulations already introduced: single-plane, multi-plane, and 3-D. The analysis is conducted on a Pininfarina wind tunnel vehicle parametric model, whose geometry has been defined by the SAE “Open-Jet Interference Committee” [12]. Two synchronized white noise sources have been installed on the model, one on the roof and the other on the windshield, and their signals have been acquired and processed considering the overhead array only and absence of wind.

4.2.1 Front and Lateral Array

In the first scenario, a solitary speaker is positioned on the windshield, with the front array serving exclusively for beamforming. In the 2D formulation, the calculation plane is parallel to the array plane and is located at a certain distance. Ideally, the plane would coincide with the vehicle surface; however, as illustrated in Figure 4.4, the complexity of the geometries prevents this. As previously highlighted, this can result in errors in the localization and an underestimation of the source intensity, particularly when sources are partially outside the calculation plane.

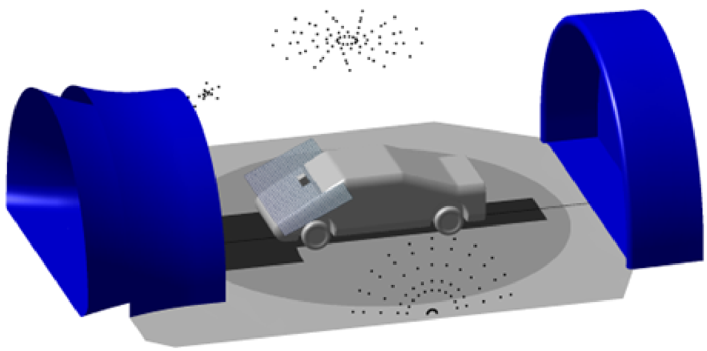

Figure 4.4: Frontal array 2-D calculation plane

As depicted by Figure 4.5, the 2-D Beamforming output seems to be weaker. The 2-D method assumes a flat surface, thus resulting in spatial inaccuracies due to its inability to adapt to the vehicle’s shape. In comparison, the 3-D formulation, which conforms to the actual geometry, eliminates these errors. As shown in Figure 4.6, it provides a more precise source representation, improving spatial accuracy and reliability. It is also noteworthy that all of the maps are shown at the same scale which makes the comparison easier.

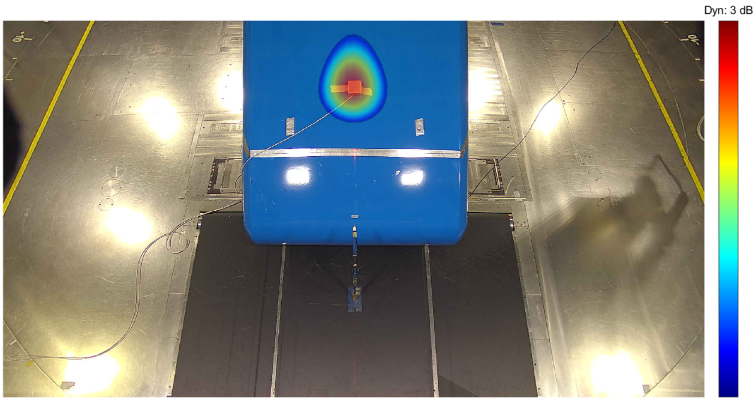

Figure 4.5: Frontal array 2-D Beamforming at 2500 Hz in the third-octave band

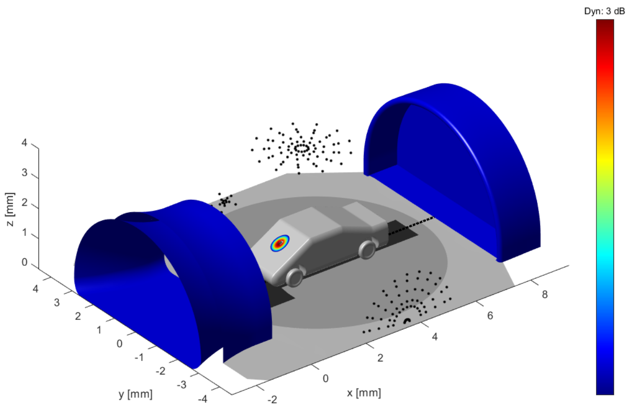

Figure 4.6: Frontal array 3-D Beamforming at 2500 Hz in the third-octave band

In the second case, the considerations are analogous to those previously discussed. A solitary speaker is positioned on the side door, with the side array employed for beamforming analysis. As previously outlined, in the 2D formulation, the calculation plane is assumed to be parallel to the array plane and fixed at a predetermined distance. This results in localization errors and underestimation of source intensity, especially when the source is partially outside the calculation domain. The effect is evident in Figure 4.7, where the 2D beamforming result appears attenuated due to the flat-surface assumption. In contrast, the 3D formulation (Fig. 4.8), which conforms to the actual geometry, effectively mitigates these errors, yielding a more accurate representation of the source.

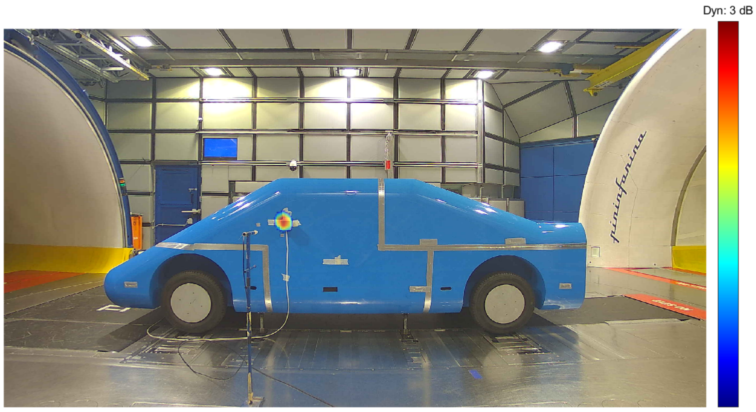

Figure 4.7: Side array 2-D Beamforming at 2500 Hz in the third-octave band

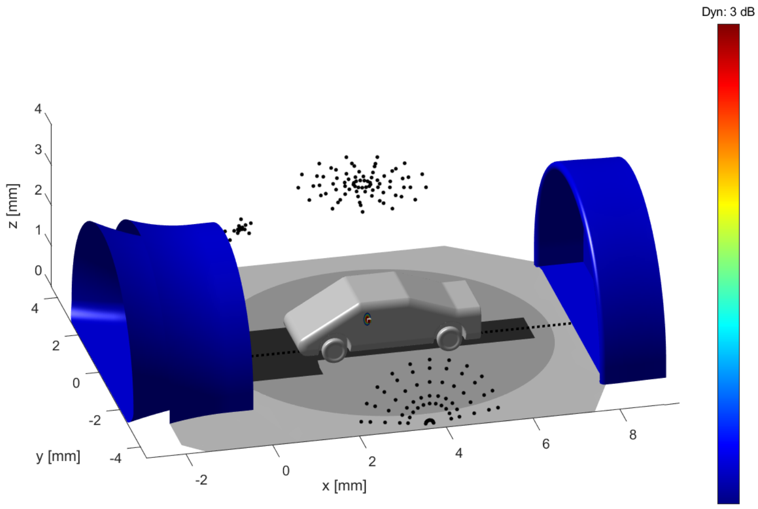

Figure 4.8: Side array 3-D Beamforming at 2500 Hz in the third-octave band

4.2.2 Top Array

In the third case, two synchronized white noise sources were installed on the model, one on the roof and the other on the windshield, and their signals were recorded and processed considering the overhead array only in the absence of wind. All the maps have the same scale to facilitate comparison.

The single-plane approach facilitates precise focusing on a specific acoustic source through the alignment of a calculation plane at a designated location, as illustrated in Figures 4.9 and 4.10. These figures depict the beamforming outcomes for the 2500-Hz one-third octave band, demonstrating that this method effectively highlights the source within the selected plane but fails to capture sources outside it. For instance, if the calculation plane is aligned with the roof source (Fig. 4.9) , the contribution from the windshield source is substantially underestimated, and the reverse is equally true (Fig 4.9).

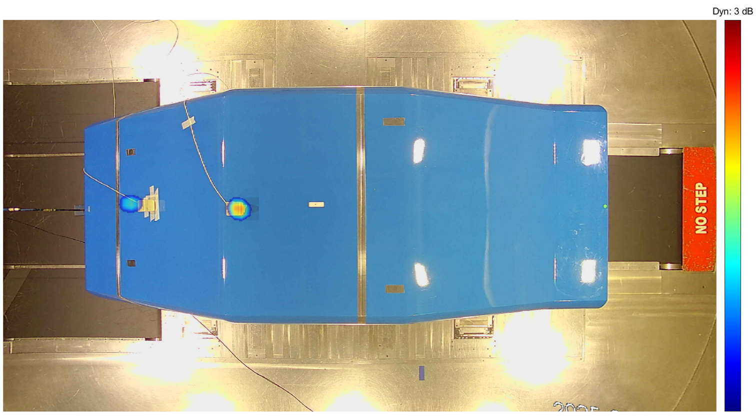

Figure 4.9: Conventional Beamforming results for the 2500 Hz one-third octave band; calculation plane aligned with the roof

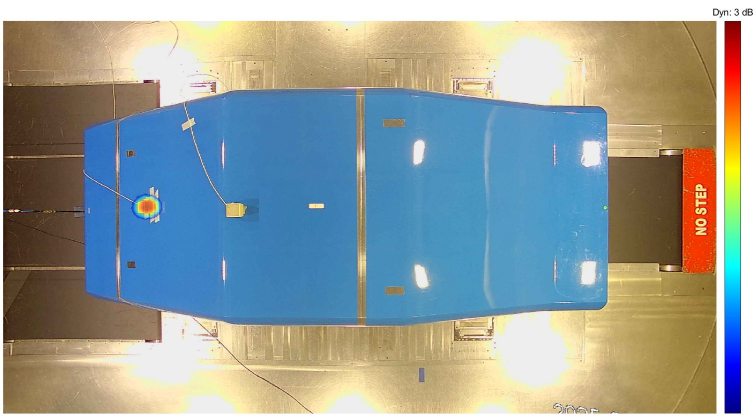

Figure 4.10: Conventional Beamforming results for the 2500 Hz one-third octave band; calculation plane aligned with the windshield

In order to address this issue, the multi-plane formulation extends the 2D approach by incorporating multiple parallel calculation planes (see Figure 4.11). This method significantly reduces underestimation errors by allowing a more accurate representation of sources at different heights. However, as depicted in Figure 4.12, while source strength estimation improves, localization inaccuracies may persist. These errors stem from the assumption that the source distribution is confined to a set of discrete planes rather than a complex surface.Similar to the front array case, the inability of the 2D method to conform to the vehicle's geometry introduces spatial deviations in the estimated source positions.

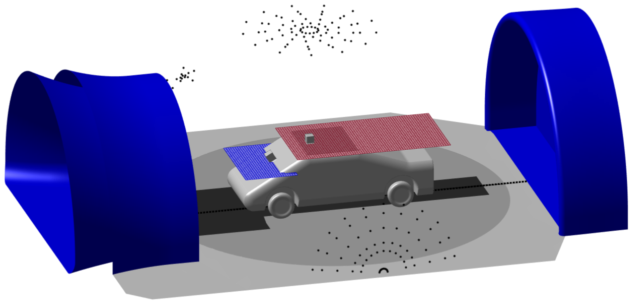

Figure 4.11: Multi-plane 2-D Beamforming calculation planes

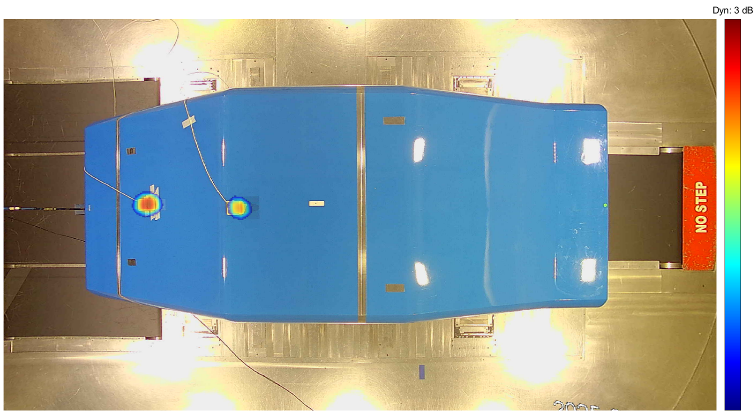

Figure 4.12: Multi-plane 2-D Beamforming approach for the 2500 Hz one-third octave band

The 3-D formulation builds upon the multi-plane approach by incorporating an infinite number of planes, thereby fully conforming to the vehicle's geometry. As shown in Figure 4.13, this approach eliminates both localization and intensity estimation errors, ensuring precise and reliable acoustic characterization.

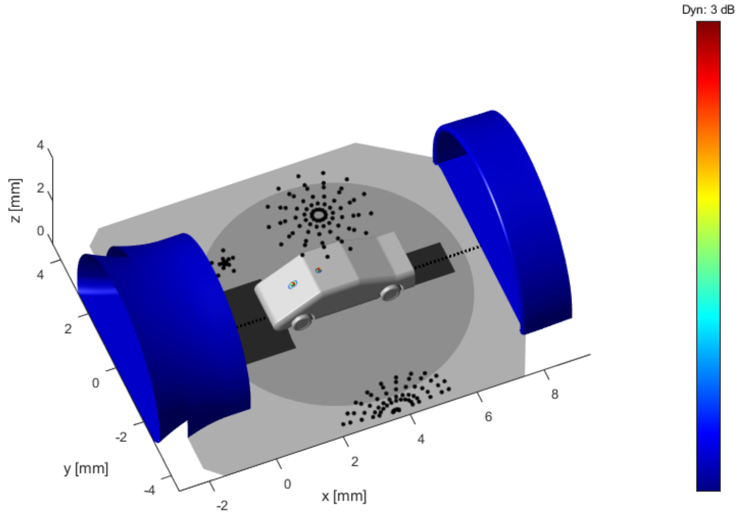

Figure 4.13: 3-D Beamforming results for the 2500 Hz one-third octave band

The model presented here is intended to demonstrate the advantages of three-dimensional mapping, without emphasising the limitations of a single microphone array. Because of the simplicity of the model, the grid points captured by the overhead array resulted in a scanning grid that is closely aligned with the vehicle's upper surface, with minimal extension in the direction normal to the array.

In real-world scenarios involving more intricate geometries, the scanning grid obtained from the overhead array would demonstrate greater height variation, resulting in iso-contour noise maps that are substantially elongated in the direction perpendicular to the array. As discussed in section2.2.3, a potential solution to this limitation is to employ the Multiplicative Beamforming technique, which integrates the information from different arrays into a unified map, thereby enhancing the spatial resolution. This approach will be discussed in the next paragraph, using a production vehicle at various wind speeds as a case study.

Chapter 5

Real Case

This section presents the experimental findings obtained by applying the 2D and 3D Conventional Beamforming and Multiplicative Beamforming algorithms to a production vehicle equipped with luggage bars. The vehicle was tested under various wind speeds.

The investigation followed a standard setup used in aeroacoustic research, where the vehicle was precisely positioned within the test section of the wind tunnel. It was aligned with the streamwise centreline to ensure optimal exposure to the airflow, and both the wheels and the floor were kept stationary throughout the experiment to maintain a controlled testing environment. The static configuration is crucial for accurately simulating a vehicle's aeroacoustic behaviour, as opposed to aerodynamic experiments, where components like the Wheel Drive Units (WDU) and the moving belt system are in motion. In static aeroacoustic tests, these elements are kept stationary, preventing extraneous noise generation. Keeping all components stationary ensures that the recorded sound data accurately reflects the vehicle's true acoustic signature, without contamination from mechanical noise.

The data acquisition process involved the utilisation of microphone arrays, with recordings lasting $T = 6.25$ seconds at a high sampling frequency of $fs = 32768\ Hz$. This high sampling rate ensured the capture of even the most subtle acoustic details with precision. Furthermore, to facilitate clear and direct comparisons across different tests, all the maps corresponding to the same one-third octave band were generated using an identical scale.

5.1 Conventional 2D Beamforming

The initial scenario under consideration is that of the vehicle being struck by a wind at 60 km/h. At this speed, the roof bars were identified as a significant contributor to the generation of aerodynamic noise. This is clearly demonstrated by the Conventional Planar Beamforming results applied to both the overhead and side microphone array, as shown in Figures 5.1 and 5.2. In particular, the left front bar support stands out as a dominant noise source and plays a key role in shaping the overall acoustic signature of the vehicle. However, it is important to note that this beamforming approach can introduce typical two-dimensional errors. These inaccuracies arise when the chosen computational plane does not coincide with the actual position of the noise source, potentially leading to errors in both the localisation and intensity estimation of the source.

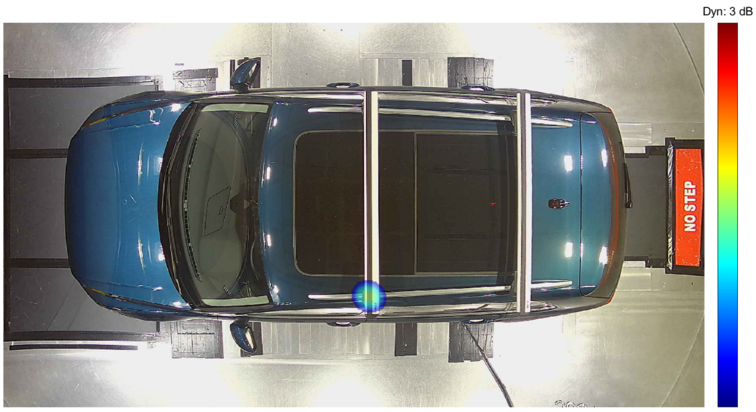

Figure 5.1: Conventional planar Beamforming results using the overhead arrays for the 1600 Hz one-third octave band

Figure 5.2: Conventional planar Beamforming results using the side arrays for the 1600 Hz one-third octave band

5.2 Conventional 3D Beamforming and Multiplicative Beamforming

Subsequent to the analysis of the aforementioned scenario, the 3-D Beamforming technique was employed, for which a 3-D scan of the vehicle was conducted.

The initial phase of the analysis employed Conventional 3-D Beamforming using two distinct planar microphone arrays: the overhead and the side array. The grid points captured by each array were included in the analysis to create a detailed acoustic map of the vehicle. However, planar arrays inherently exhibit anisotropic spatial resolution, meaning that they provide high resolution along the plane of the array but have significantly limited resolution in the direction perpendicular to that plane. Consequently, accurately localising the noise sources remains challenging, necessitating further refinement of the beamforming technique to overcome these spatial limitations.

As illustrated in Figure 5.3, the conventional beamforming outcomes derived from the overhead array for the 1600-Hz one-third octave band are presented. This representation demonstrates that the overhead array exhibits a remarkably narrow beamwidth along directions parallel to its plane, indicative of a high level of resolution and enabling precise localization of sound sources. Conversely, in the direction perpendicular to the plane, the beam becomes elongated, indicating a marked reduction in resolution and making depth localization more challenging.

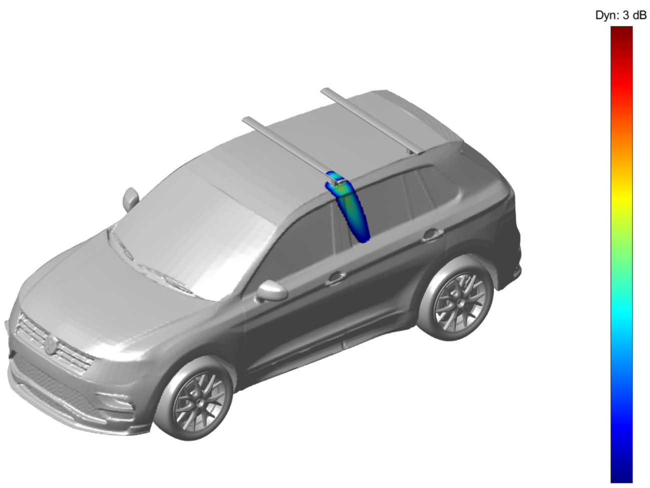

Figure 5.3: Conventional 3D Beamforming results using the overhead arrays for the 1600 Hz one-third octave band

A comparable pattern should be observed for the side array, as shown in Figure 5.4. However, its calculation plane does not extend as far in the perpendicular direction, which slightly alters the resolution characteristics observed in that orientation.

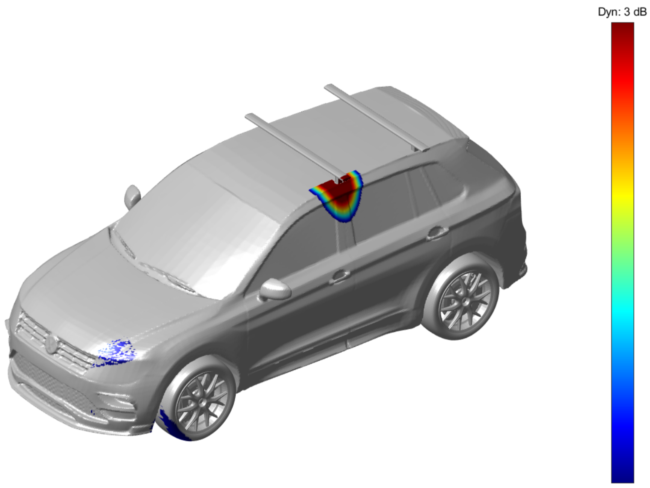

Figure 5.4: Conventional 3D Beamforming results using the side arrays for the 1600 Hz one-third octave band

In order to address the limitations previously discussed, the Multiplicative Beamforming technique was introduced as a refined method to enhance localization accuracy. This innovative approach takes full advantage of the spatial complementarity offered by two mutually orthogonal arrays.Initially, Conventional Beamforming is applied separately to the overhead and the side arrays, generating individual acoustic maps that capture the unique strengths of each configuration. These maps are then combined through a pointwise multiplication process, which retains the high-resolution details inherent in each array while simultaneously mitigating the adverse effects associated with low-resolution regions.This multiplication reinforces the precise localization of sound sources along the array planes and compensates for the directional disparities, resulting in a more isotropic localization map.As illustrated in Figure 5.5, the final source map demonstrates a uniform spatial resolution that is free from any directional bias. Although some side lobes remain visible, they are significantly reduced compared to the outputs produced by Conventional Beamforming alone, thereby providing a much clearer and more reliable representation of the acoustic field.

Increasing the wind tunnel flow speed to V = 120 km/h reveals additional noise sources that were not as apparent at lower speeds. Notably, the vehicle's front grille begins to emit a distinct tonal noise, which is clearly evident in the 2500 Hz one-third octave band.Due to the specific location of this source, the Multiplicative Beamforming algorithm was adapted to incorporate data from both the front and the overhead microphone arrays. This dual-array approach is predicated on the complementary spatial information provided by each array, thus resulting in a more precise and robust localization of the tonal emission. The enhanced acoustic map, as demonstrated in Figure 5.6, clearly delineates the source location, thereby demonstrating the effectiveness of this technique in isolating and accurately characterising noise contributions at higher wind speeds.

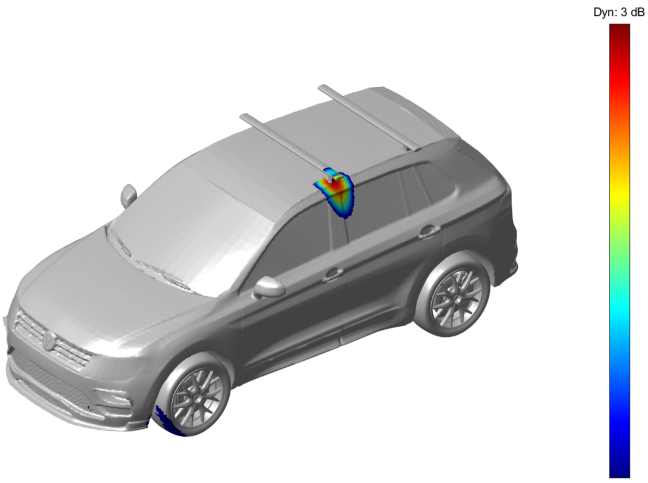

Figure 5.5: Multiplicative Beamforming results obtained considering overhead and side arrays for the 1600 Hz one-third octave band

Figure 5.6: Multiplicative Beamforming results obtained considering front and overhead arrays for the 2500 Hz one-third octave band

Chapter 6

Conclusion

This study proposes a pioneering three-dimensional (3D) beamforming algorithm that signifies a substantial advancement in the domain of vehicle aeroacoustic research. In contradistinction to conventional methodologies, this novel approach directly maps noise sources onto the vehicle surface, thereby facilitating a more intuitive and precise visualisation of the acoustic energy generation. By integrating data from multiple microphone arrays into a unified acoustic map, the proposed multiplicative beamforming technique successfully circumvents the inherent limitations associated with conventional planar and multi-plane beamforming methods.

A detailed comparative analysis revealed that conventional 2-D beamforming techniques often suffer from localization errors and intensity distortions, primarily due to focus deviations, particularly when dealing with noise sources that lie out of the measurement plane. In contrast, the advanced 3-D approach effectively mitigates these issues by accounting for the complex geometry of the vehicle. This approach ensures that noise source localization is not only more precise but also more reflective of the true spatial distribution of acoustic emissions across the vehicle's body.

Furthermore, the implementation of the Multiplicative Beamforming method has been demonstrated to enhance spatial resolution by leveraging the complementary strengths of diverse microphone arrays. Through the integration of data from these arrays, the algorithm facilitates the identification of noise sources with enhanced reliability and robustness. This enhancement in spatial resolution results in an acoustic map that offers a more precise and detailed depiction of noise distribution, a critical aspect for both diagnostic purposes and the subsequent development of noise reduction strategies.

The validity of the proposed technique was further substantiated through real-world testing on a production vehicle. The method demonstrated its capacity to accurately detect and localise noise sources under various wind speeds, thus underscoring its practical applicability. This enhanced resolution and source mapping capability positions the technique as a potent tool for optimising vehicle acoustic performance. This is particularly salient in the contemporary automotive landscape, where the reduction of wind noise is of paramount importance, especially for electric vehicles that often feature quieter powertrains.

6.1 Future works

Subsequent research efforts will be dedicated to refine the algorithmto further increase spatial resolution and computational efficiency. This will involve optimizing 3D vehicle scanning techniques and minimizing processing time to align with wind tunnel testing requirements.

Moreover, there is considerable scope for extending the application of this method to more intricate vehicle configurations. The integration of the algorithm with other advanced noise reduction strategies could yield even more profound insights, providing automotive manufacturers with a valuable resource in their endeavours to enhance cabin comfort and overall vehicle performance.

Bibliography

[1] Leandro de Santana. «Fundamentals of Acoustic Beamforming». In: *Department Thermal Fluid Engineering University of Twente* (2017) (cit. on pp. 1, 2, 21, 22).

[2] Ennes Sarradj. «Three-Dimensional Acoustic SourceMapping with Different Beamforming Steering Vector Formulations». In: *Department of Technical Acoustics, Brandenburg University of Technology* (2012) (cit. on pp. 2, 24).

[3] R. Arina. *Slides del corso di aeroacustica*. Politecnico di Torino, 2024 (cit. on p. 7).

[4] Allan D. Pierce. *Acoustics: An Introduction to Its Physical Principles and Applications*. Acoustical Society of America, 1989 (cit. on p. 8).

[5] S. Glegg and W. Devenport. *Aeroacoustics of Low Mach Number Flows*. Academic Press of Elsevier, 2017 (cit. on pp. 9, 11, 13, 16, 18, 19, 21).

[6] Michael Brandstein and Darren Ward. *Microphone Arrays: Signal Processing Techniques and Applications*. Springer, 2001 (cit. on p. 17).

[7] P. M. Morse and K. U. Ingard. *Theoretical Acoustics*. Princeton University Press, 1968 (cit. on p. 17).

[8] J.J. Christensen and J. Hald. *Beamforming*. Tech. rep. Brüel&Kjær, 2004 (cit. on pp. 21–24, 30).

[9] R. Porteous, Z. Prime, V. Valeau, C. Doolan, and D. Moreau. «Three-dimensional beamforming of aeroacoustic sources». In: *Inter-noise* (2014) (cit. on pp. 25, 36).

[10] Francesco Uffreduzzi, Alessandro Aquili, and Raj Mattias Mehta. «Coherence-based Beamforming algorithm for vehicle cabin acoustic comfort evaluation». In: *Rivista Italiana di Acustica v. 48, n. 1* (2024) (cit. on p. 28).

[11] Johnson D. H. and Dudgeon D. E. *Array Signal Processing: Concepts and Techniques*. P T R Prentice Hall, 1993 (cit. on pp. 29, 30).

[12] A. Cogotti. «A Parametric Study on the Ground Effect of a Simplified Car Model». In: *SAE International, Warrendale, PA, SAE Technical Paper 980031,* (1998) (cit. on p. 40).